Evidence for a large-magnitude Holocene eruption of Mount Rittmann (Antarctica): a volcanological reconstruction using the marine tephra record

Di Roberto A.[a], Albert P.G.[b,c], Colizza E.[d], Del Carlo P.[a], Di Vincenzo G.[e], Gallerani A.[f], Giglio F.[g], Kuhn, G.[h], Macrì P.[i], Manning C.J.[l], Melis R.[d], Miserocchi S.[g], Scateni B.[a], Smith V.C.[c], Torricella F.[m], Winkler A.[i]

a - Istituto Nazionale di Geofisica e Vulcanologia, Sezione di Pisa, Via C. Battisti 53, 56125 Pisa, Italy
b – Department of Geography, College of Science, Swansea University, Singleton Park, Swansea, SA2 8PP, UK
c - Research Laboratory for Archaeology and the History of Art, 1 South Parks Road, University of Oxford, OX1 3TG, UK
d - Dipartimento di Matematica e Geoscienze, Università di Trieste, Via E. Weiss 2, 34127 Trieste, Italy
e - Consiglio Nazionale delle Ricerche - Istituto di Geoscienze e Georisorse (CNR-IGG), Via G. Moruzzi 1 56124 - Pisa, Italy
f - Consiglio Nazionale delle Ricerche - Istituto di Scienze Marine (CNR-Ismar), Via Gobetti 101 40129 Bologna, Italy
g - Istituto di Scienze Polari - Consiglio Nazionale delle Ricerche ISP-CNR, Via P. Gobetti 101, 40129, Bologna, Italy
h – Alfred-Wegener-Institut Helmholtz-Zentrum für Polar- und Meeresforschung, Am Alten Hafen 26, D-27568, Bremerhaven, Germany
i-Istituto Nazionale di Geofisica e Vulcanologia, Sezione di Roma 2, Via di Vigna Murata 605, 00143 Roma, Italy
l - Department of Earth Sciences, Royal Holloway University of London, Queen's Building, Egham TW20 0EX, UK
m - Dipartimento di Scienze della Terra, Via Santa Maria, 53, 56126 Pisa, Italy

Abstract

In Antarctica, the near-source exposures of volcanic eruption deposits are often limited as they are not well preserved in the dynamic glacial environment, thus making volcanological reconstructions of explosive eruptions extremely challenging. Fortunately, pyroclastic deposits from explosive eruptions are preserved in Southern Ocean sediments surrounding Antarctica, and the tephrostratigraphy of these sequences offers crucial volcanological information including the timing and tempo of past eruptions, their magnitude, and eruption dynamics. Here we report the results of a

tephrostratigraphy and tephrochronology study focused on four sediment cores recovered from the Wood Bay area in the western Ross Sea, Antarctica. In all these sedimentary sequences, we found a well-stratified primary tephra of considerable thickness, up to 80 cm, hereafter named the Aviator Tephra (AVT). According to the characteristics of the tephra deposit and its distribution, the AVT was associated with an eruption of considerable intensity, potentially representing one of the largest Holocene eruptions recorded in Antarctica. Based on the major and trace element geochemistry and the mineral assemblage of the tephra, Mount Rittmann was identified as the source of the AVT. A Holocene age of ~ 11 ka was determined by radiocarbon dating organic material within the sediments and ^{40}Ar-^{39}Ar dating of alkali-feldspar crystals included in the tephra. Eruption dynamics were initially dominated by hydromagmatic magma fragmentation conditions producing a sustained, relatively wet and ash-rich eruptive cloud. The eruption then evolved into a highly energetic, relatively dry magmatic Plinian eruption. The last phase was characterized by renewed efficient magma-water interaction and/or collapse of the eruptive column producing pyroclastic density currents and associated co-ignimbritic plumes. The distal tephra deposits might be linked to the widespread lag breccia layer previously identified on the rim of the Mount Rittmann caldera which share the same geochemical composition. Diatoms found in the sediments surrounding the AVT and the primary characteristics of the tephra indicate that the Wood Bay area was open sea at the time of the eruption, which is much earlier than previously thought. AVT is also an excellent tephrostratigraphic marker for the Wood Bay area, in the Ross Sea, and a useful marker for future synchronization of continental ice and marine archives in the region.

1. Introduction

Tephrochronology has been widely used in Antarctica as a dating and correlation tool. Tephra detected within ice sequences have been exploited for the correlation and the synchronization of glacial archives (Dunbar and Kurbatov, 2011; Narcisi et al., 2017, 2012; Palais et al., 1987). Although

numerous tephra have been found intercalated with glaciomarine sediments of the Southern Ocean surrounding Antarctica, only a few specific studies were dedicated to their characterization (Antoniades et al., 2018; Colizza et al., 2003; Del Carlo et al., 2015; Di Roberto et al., 2019, 2020; Hillenbrand et al., 2008; Licht et al., 1996; Moreton and Smellie, 1998; Oppedal et al., 2018; Smellie 1999).The results of this study have demonstrated that tephra deposits recovered from marine sediments are an important resource to reconstruct past volcanism. Indeed, studies on offshore sequences around Antarctica have considerably increased the number of known eruptions. This is because only 1% of the total land area on the continent is ice-free (Burton-Johnson et al., 2016) and the dynamic glacial environments do not preserve tephra sequences. In these terms, marine tephra record is of fundamental importance to build a complete representation of the explosive volcanic activity through time, including source, magnitude, chemical evolution, and dynamics of the eruption. Like tephra in ice archives, those recognized in marine sequences represent invaluable isochrons for dating and correlating the records and the synchronization of climate proxy records. The recent discovery of the 1254 C.E. tephra at Edisto Inlet (Di Roberto et al., 2019; Tesi et al., 2020), deriving from Mt. Rittmann volcano, has allowed, for the first time in Antarctica, the unequivocal, independent time-stratigraphic correlation and synchronization between continental ice-archives and marine sediments. These correlations are fundamental for understanding the nature of connections and coupling processes between atmospheric, ice-sheets, ocean dynamics, marine sedimentary systems and climate changes (Di Roberto et al., 2019).

This paper reports the results of tephrostratigraphy and tephrochronology studies carried out on a thick tephra layer identified in four sediment cores recovered from the Wood Bay area in the Ross Sea, Antarctica (Fig. 1). We include the textural, mineralogical and geochemical (major and trace element glass) information of tephra found in the marine sediments. We report geochronological constraints on the eruption deposits including an ^{40}Ar-^{39}Ar age for the tephra and ^{14}C dates from the host sediments. We also use the lithologic features of the tephra to gain insight into the emplacement dynamics and paleoenvironmental conditions at the time of deposition.

2. Volcanological background

Melbourne Volcanic Province comprises six relatively young volcanic complexes associated with north to NW-trending grabens and faults in Northern Victoria Land (LeMasurier et al., 1990). From south to north these are Mount Melbourne, Mount Overlord (including Mount Rittmann), Malta Plateau, The Pleiades, and Vulcan Hills volcanic fields (Fig. 1). Some of these volcanoes show evidence of recent activity, with fumaroles or tephra exposed on their flanks, and considered as possible sources of tephra identified in the Victoria Land area and the Ross Sea sediments. Here, we describe eruptive centers that according to the available literature have been active during the late Pleistocene and Holocene which represent the likely volcanic sources for the tephra layers recovered in studied marine sediment cores.

The Mount Melbourne volcanic field comprises its prominent stratovolcano that is 2,732 m-high, and has a basal diameter of ca. 21-24 km, several subglacial vents aligned in N-S direction, and a number of small scoria cones, domes, lava flows, and lava fields (Giordano et al., 2012). According to these authors, Mount Melbourne volcano has been very active since ~150 ka and recent activity is confirmed by the presence of several tephra layers in the surrounding ice cliffs (Lyon, 1986) and active fumaroles located along a N-S line cutting through the summit and along a line of phreatomagmatic craters on the southern rim. The youngest englacial tephra found in ice cliffs and ice tongues of the Tinker and Aviator glaciers was attributed to an eruption that possibly occurred in the period 1862-1922 (Adamson and Cavaney, 1967; Nathan and Schulte, 1968). The thick volcanic deposits that outcrop in different portions of the edifice mainly consist of trachytic ignimbrites (123.6 ± 6.0 ka; Giordano et al., 2012), and alkali basaltic, hawaiitic and subordinate benmoreitic lavas and scoria cones (90.7 ± 19.0 ka; Giordano et al., 2012). The most recent products of Mount Melbourne are exposed widely on the edifice and consist of trachytic to rhyolitic pumice fall deposits likely originated from Plinian eruptions (Giordano et al., 2012).

Mount Rittmann volcano is included in the Mount Overlord volcanic field (Armienti and Tripodo, 1991). Active fumaroles and summit geothermal activity suggest that the volcano is still active (Bonaccorso et al 1991). Mount Rittmann is represented by volcanic rock exposures that appear to be related to a remnant of a roughly 8 x 5 km wide caldera. The rocks are mainly trachytic lavas, less hawaiite scoria, and rarely mugearite, benmoreite and phonolite (Armienti and Tripodo, 1991). The volcanic activity of Mount Rittmann occurred between the Pliocene and the Holocene (Armienti and Tripodo, 1991) but the most recent activity is poorly known. Mount Rittmann is also considered the source of tephra and cryptotephra layers found in many of the ice-cores drilled in Antarctica. In particular Mount Rittmann was recently proposed as the source for a widespread tephra found in five ice cores from East and West Antarctica at Brimstone Peak (BIT106; Dunbar, 2003), in Siple B and Taylor ice cores (Siple B 97.2 e 97.45 and Taylor 79.155; Dunbar et al., 2003), in Talos Dome ice core (TD87a; (Narcisi et al., 2012), in WAIS core WDC05-190.80 and 190.37 (Sigl et al., 2016) and in Rice core AnT16 (Iverson et al., 2017). Recently the 1254 C.E. cryptotephra was recognized within marine sediments close to Cape Hallett (northern Victoria Land), in the western Ross Sea, Antarctica (Di Roberto et al., 2019; Tesi et al., 2020).

The Pleiades volcanoes consist of the small trachytic Mount Pleiones/Atlas volcano and a number of lava domes and scoria cones that have been repeatedly active over the last 100 ka (Esser and Kyle, 2002). The Pleiades were considered the youngest volcanic centers in the Northern Victoria Land based on the geomorphological expression (Nathan and Schulte, 1968; Riddolls and Hancox, 1968) and geochronology data (Esser and Kyle, 2002). ^{40}Ar-^{39}Ar and K-Ar ages of ~3 ka (and 6±6 ka) were obtained from the Taygete cone NNE of Mount Pleiones (Esser and Kyle, 2002; Kyle, 1990). The occurrence of hydrothermal activity (no longer active; Esser and Kyle, 2002; Fraser et al., 2014) and the widespread pumice lapilli fallout deposits on the surface of The Pleiades provide evidence for Holocene volcanic activity. Deposits from the Pleiades consist of rocks belonging to the alkali-rich basanite-tephrite-phonotephrite-phonolite suite (Kyle, 1990) and an alkali-poorer suite of hawaiites, mugearites, benmoreites, and trachytes (Kyle, 1990). The volcanic rocks were subdivided into two

magmatic lineages based on petrography and whole-rock compositions (Kim et al., 2019): a sodic silica-undersaturated lineage with the rocks containing abundant kaersutite phenocrysts, and a potassic and mildly-alkalic, silica-saturated to slightly undersaturated lineage containing olivine phenocrysts with the latter that constitutes the majority of the eruptive volume (Kyle and Rankin, 1976).

3. Materials and Methods

We investigated four cores recovered in the Wood Bay sea (ANTA02-AV43, ANTA02-AV45, TR17-05PC, and TR17-12PC; Figs. 1-3; Table 1) that is located along the western coast of the Ross Sea, in front of the Aviator Ice tongue (Fig. 1). The bay morphology is characterized by a narrow basin, deeper than 1000 m, oriented WNW-ESE, and transversally connected, by an 800 m-deep sill, to the Drygalski basin, that stretches NE-SW (Fig. 1). Seismic profiles, acquired in the bay, show wide areas covered by transparent acoustics, which are interpreted as Holocene sediments and characterized by closely laminated diatom ooze (Colizza et al., 2003; Mezgec et al., 2017). The ANTA02-AV43 core, previously studied by (Del Carlo et al., 2015) has been reviewed and partially re-analyzed in this work. Cores ANTA02-AV45 and TR17-05PC are characterized by a similar lithological organization consisting of glaciomarine diamicton at the base overlain by variable thickness of organized tephra (Figs. 2 and 3). The sediment above the tephra layers is characterized by hydrated weakly laminated diatomaceous ooze with scattered ice-rafted debris more concentrated at the base of the unit. In cores ANTA02-AV43 and TR17-12PC, the tephra layer characterizes the base of the cores (no glaciomarine diamicton occur at the base of the core), and the above sediment is a very hydrated slightly bioturbated diatomaceous ooze with few scattered pieces of ice-rafted debris (Figs. 2 and 3).

3.1. Glass texture, mineral assemblage, and geochemistry

Visible tephra layers identified in the studied cores were described, sub-sampled, mounted with epoxy resin, and prepared for textural, petrographical, and geochemical analyses (major and trace elements). The texture of volcanic particles and the composition of minerals were studied using a scanning electron microscope (SEM), Zeiss EVO MA at the Istituto Nazionale di Geofisica e Vulcanologia, Sezione di Pisa (INGV-Pisa). Major and minor element volcanic glass chemistry of individual juvenile clasts from the marine tephra deposits were determined on polished surface using a wavelength-dispersive JEOL 8600 electron microprobe at the Research Laboratory for Archaeology and the History of Art, University of Oxford. A beam accelerating voltage of 15kV was used with a 6nA current and a beam diameter of either 10 or 5 µm depending on the glass surface areas. The instrument was calibrated with a suite of appropriate mineral standards; peak count times were 30 s for all elements except Mn (40s), Na (12s), Cl (50s), P (60s). Reference glasses from the Max Planck institute (MPI-DING suite; Jochum et al., 2005) bracketing the possible chemistries were also analysed alongside the unknown tephras. These included felsic [ATHO-G (rhyolite)], through intermediate [StHs6/80-G (andesite)] to mafic [GOR132-G (komatiite)] glasses. All glass data has been normalised to 100 % for comparative purposes. This is of paramount importance for tephra in marine sediment cores, as glass shards absorb water from their surroundings, which often results in low totals. Analytical totals < 93 wt.% were discarded. Errors are typically < ± 0.7% RSD for Si; ~ ± 3% for most other major elements, except for the low abundance elements: Ti (~ ± 7%), Mn (~ ± 30%). Error bars on plots represent reproducibility, calculated as a 2 x standard deviation of replicate analysis of MPI-DING StHs6/80-G. The full glass dataset of the marine tephra deposits analysed and the standard data are reported in Supplementary Information 1.

Trace element analysis of volcanic glass shards was performed using an Agilent 8900 triple quadrupole ICP-MS (ICP184 QQQ) coupled to a Resonetics 193nm ArF excimer laser-ablation in the Department of Earth Sciences, Royal Holloway, University of London. Full analytical procedures used are reported in Tomlinson et al. (2010). Spot sizes 20 and 25 µm were used depending on the vesicularity, crystal content and ultimately the size of available glass surfaces. The repetition rate was

5 Hz, with a count time of 40 s on the sample, and 40 s on the gas blank to allow the subtraction of the background signal. Blocks of eight or nine glass shards and one MPI-DING reference glass were bracketed by the NIST612 glass calibration standard (GeoREM 11/2006). In addition, MPI-DING reference glasses were used to monitor analytical accuracy (Jochum et al., 2006). The internal standard applied was 29Si (determined by EPMA analysis). LA-ICP-MS data reduction was performed in Microsoft Excel. Accuracies of LA-ICP-MS analyses of MPI-DING glass standards ATHO-G and StHs6/80-G were typically ≤ 5%. Full glass datasets and MPI-DING standard glass analyses are provided in Supplemental Material 1.

Similarity Coefficient index (SC; Sarna-Wojcicki et al., 1987) and statistical distance (D_2; Perkins et al., 1995) were used to assess the potential correlations. The SC is calculated as the average of ratios of elemental concentrations between pairs of compositional analyses of tephra (calculated as averages). Two samples are considered as correlatives if they have an SC value close to 1, with SC > 0.92 considered as a lower bounding value for a good statistical correlation. By contrast, statistical distance (D_2) measures the difference between two tephra based on their average compositions and standard deviations. D_2 is a distance function, thus the lower its value the higher is the similarity between two samples being compared. Compositionally identical samples have $D_2 = 0$. The use of these SC and D_2 indices is not without problems but in general, the indices are widely used and give a broad numerical-strength indication of the compositional similarity between two samples.

3.2. Radiocarbon and ^{40}Ar-^{39}Ar age determination

The age depth models of the cores are based on 12 new accelerator mass spectrometry (AMS) radiocarbon dates measured at the Foundation of the Poznań Radiocarbon Laboratory, Poland and with a MICADAS (Wacker et al., 2013) at Alfred-Wegener-Institut Helmholtz-Zentrum für Polar- und Meeresforschung (AWI). Two radiocarbon dates from Colizza et al. (2004) and another one from Mezgec et al. (2017) were included in the data set. Radiocarbon dates were all performed on the acid-insoluble organic fraction (AIO) from bulk sediment samples (Table 2). Radiocarbon chronologies

using the AIO fraction from bulk sediments are often compromised by contamination from reworked ancient organic carbon derived from glacial erosion and/or from the reworking of unconsolidated sediments (see Mezgec et al., 2017 for the discussion). This is evidenced by AIO dates of Antarctic surface sediments that extend over several thousand years (Andrews et al., 1999; Pudsey et al., 2006). Unfortunately, we cannot correct these errors using the age of surface sediments from the studied cores, as commonly done; in fact, the piston coring system with which the cores were sampled did not preserve the water/sediment interface. Thus, we used the uncorrected ages obtained from superficial sediments sampled in the same area by box coring (that preserves the water/sediment interface) to correct the TR17-12PC, ANTA02-AV43 and ANTA02-AV45 core ages (BAY05-bc40; see Mezgec et al., 2017), and TR17-05PC ones (box core TR15-05bc). Part of these old ages is also attributed to the marine reservoir effect (MRE). The MRE in Antarctic areas is in the range 0.75-1.3 ka ^{14}C (see discussion in Hillenbrand et al., 2010), but for the treatment of data here presented, we used a regional MRE of 1.14 ± 0.12 ka ^{14}C that was suggested by Hall et al. (2010) for the Ross Sea. We assumed that the age differences between the uncorrected ^{14}C ages of the surface sediments samples taken from the studied cores and the MRE are due to local contamination from older organic matter, and hereafter referred to as "local contamination offset" (LCO, see discussion in Hillenbrand et al., 2010). Before calibrating the ^{14}C dates, the LCO obtained for these sites was subtracted from the conventional ^{14}C down core ages of the relative cores (corrected ages), assuming that both MRE and LCO did not change over the Holocene (Hall et al., 2010). The corrected AMS ^{14}C dates were converted into calibrated ages using the CALIB REV 7.1.0 calibration program (Stuiver et al., 2019), the Marine13 (100%) calibration curve and assuming regional marine offset (ΔR) 0.79 ± 0.12 ka from the global MRE, according to Hall et al. (2010). The conventional corrected and calibrated AMS ^{14}C data are reported in Table 2 along with the sedimentation rates expressed in cm/year. The ages between dated levels were interpolated assuming a linear sedimentation rate.

The ^{40}Ar-^{39}Ar analyses of alkali feldspar extracted from the tephra layer were completed at IGG-CNR (Pisa). The mineral separates (grain size >500 μm) were leached in an ultrasonic bath at room

241 temperature for a few minutes in diluted HF (7 %) and subsequently wrapped in aluminum foil and
242 irradiated for 2 h in the core of the TRIGA reactor at the University of Pavia (Italy) along with the
243 Alder Creek sanidine (ACs) standards. Single grains were placed into 1.5 mm diameter holes of a
244 copper holder, loaded into a vacuum chamber comprising a laser port consisting of a ZnSe window
245 fitted with a differentially pumped flange, and baked for 12 h at 150°C. Total fusion experiments
246 were performed using a CO_2 laser beam (New Wave Research MIR10–30 CO_2 laser system)
247 defocused to a ~1 mm spot size. Step-heating experiments were attempted on two single grains and
248 one multigrain aliquot, the latter using grains with comparable morphology, with the laser beam
249 defocused to 2-mm spot size. Steps were carried out at increasing laser power until complete melting
250 occurred. Extracted gases were purified in a low volume stainless steel inlet system for 5 min
251 (including 30 s of lasering), using three SAES NP10 getters (one held at ~400° C and two at room
252 temperature). Argon isotope measurements were performed simultaneously in static mode using an
253 ARGUS VI (Thermo Fisher Scientific) multicollector mass spectrometer. The ^{36}Ar was measured
254 using a Compact Discrete Dynode (CDD) detector and the remaining Ar isotopes using Faraday
255 detectors, equipped with 10^{12} Ω resistors for ^{40}Ar and ^{38}Ar and 10^{13} Ω resistors for ^{39}Ar and ^{37}Ar.
256 Faraday detectors were cross calibrated for the slight offset with ~4000 fA air shots. The CDD was
257 calibrated daily for its yield by measuring four to six air pipettes prior to the first analysis. Mass
258 discrimination was determined overnight and during sample measurements based on automated
259 analyses of air pipettes. Blanks were monitored every one to two runs and were subtracted from
260 succeeding sample results. The correction factors for interfering isotopes from K and Ca were based
261 on long-term determinations on K-rich and Ca-rich glasses (uncertainties ±1σ): $(^{40}Ar/^{39}Ar)K$ =
262 0.00969 ± 0.00077, $(^{38}Ar/^{39}Ar)_K$ = 0.01283 ± 0.00012, $(^{39}Ar/^{37}Ar)_{Ca}$ = 0.000718 ± 0.000034 and
263 $(^{36}Ar/^{37}Ar)_{Ca}$ = 0.000255 ± 0.000024. Uncertainties on total gas ages, on error-weighted mean ages
264 also include the uncertainty in the fluence monitor and are given at 2σ. Ages were calculated relative
265 to an ACs age of 1.1848 Ma (Niespolo et al., 2017), using decay constants of Steiger and Jäger (1977),
266 and an atmospheric $^{40}Ar/^{36}Ar$ ratio of 298.56 ± 0.31 (Lee et al., 2006). Data are reported in Table 3.

Argon isotope concentrations are reported as relative abundances and have been corrected for blank, mass discrimination, and radioactive decay.

3.3. Diatom assemblages

The diatom assemblages were studied in close proximity of the tephra layer (28 samples, Table 4) to derive information on climate conditions at the time of AVT tephra deposition. Sediment treatment and slide preparation followed the method described in Rathburn et al. (1997). At least 300 valves were counted with a 1000x magnification following the technique described in Crosta and Koç (2007) and Pike et al. (2009). The relative diatom abundance was determined as the fraction of diatoms species against the total diatom abundance in the sample. Total diatoms abundances (ADA) were calculated using the equation proposed by Armand, (1997) and it was expressed as the number of valves per gram of dry sediments (nv/gds). In order to directly compare our results with those from Colizza et al. (2004), we only discussed the distribution of *Fragilariopsis curta*, *Eucampia antarctica*, and *Thalassiosira antarctica*.

4. Results

4.1. Tephra lithostratigraphy

A visible tephra layer named Aviator Tephra (hereafter AVT) was identified in cores ANTA02-AV43 at 137-215 cm, ANTA02-AV45 at 161-187 cm and in cores TR17-05PC at 62.5-90.5 cm and TR17-12PC at 409-416.5 cm, core depth respectively (Figs. 2 and 3). The same tephra was recognized also in several other cores in the Aviator Basin that are not considered here because they were disturbed during the coring operations.

In cores ANTA02-AV43, ANTA02-AV45, TR17-05PC and TR17-12PC, the AVT is up to 78 cm-thick (max thickness in core ANTA02-AV43) and consists of three main lithostratigraphic units

(LSU) named A, B, and C (from the base to the top), which differ in color, grain size, and components (Fig. 4).

Lithostratigraphic unit A (LSU-A), which is at the base of the tephra, is ~64 cm-thick in core ANTA02-AV43 and only ~3 cm-thick in TR17-12PC (Fig. 2 and 3). In TR17-12PC core, the piston corer was probably not effective at penetrating this coarse-grained sediment therefore only a small part of the basal layer was recovered in this 5 m-long core. In core ANTA02-AV45 the LSU-A represents the whole tephra with a thickness of ca. 26 cm. LSU-A includes three main clast populations: 1) accretionary pellets <5 mm (Figs. 5a-d); 2) fine to very fine-ash, poorly sorted, including volcanic clasts with dense to variably vesicular glass shards, fragments of crystal-rich to holocrystalline volcanic rocks, and magmatic crystal (Figs. 5c-d); 3) moderately to high vesicular pumice with microcrystals of k-feldspar and plagioclase, spinel, amphibole, clinopyroxenes, and fayalitic olivine (Figs. 5c-d). Accretionary pellets represent the main part of the particles forming the LSU-A. Two main types of accretionary pellets have been identified: i) cored pellets formed by the accretion of multiple concentric layers of fine ash around a nucleus that is either a magmatic crystal or a vesiculated fragment (AP2 of Brown et al., 2012; Fig. 5e). Accreted layers range in thickness from few to ~150 microns and comprise alternating bands with relatively sharp contacts made of sub-micron to ~100 μm glass particles. No clear grain size/thickness pattern exists except for a final thinning and fining outward. ii) Unstructured to poorly structured aggregates formed by fine-grained ash embedding up to 150 microns particles (AP2 of Brown et al., 2012); Figs. 5f-g). Besides these two main types of aggregates, we also found: i) particles with a concentrically layered rim (AP2-like) over an AP1 aggregate which acts as the nucleus, ii) AP1 secondary unstructured coatings over an AP2 core or iii) aggregated cluster of small AP1 and AP2 type aggregates (Fig. 5h). Particles forming the coating layers and the nucleus of aggregates are often altered. Larger glassy particles are incipient to pervasively devitrified, altered to zeolite, calcite and clay minerals and vesicles are often filled with calcite. Similarly, few microns particles forming coating layers or unstructured aggregates are often incipiently altered to completely transformed into a micritic mass of clay minerals and zeolite

317 and cemented together by clay mineral, amorphous silica, and calcite (possibly derived from previous
318 cement).
319 Lithostratigraphic unit B (LSU-B, the intermediate portion of the tephra) is ~3 cm-thick in cores
320 ANTA02-AV43 and TR17-12PC. It is made of well-sorted medium ash to fine pumiceous lapilli (Fig.
321 6a). Particles forming this layer have a wide range of shapes and vesicularities, and range from grey-
322 greenish pumice up to 3-4 mm (Fig. 6a) to minor colorless-light green dense glass fragments (Fig.
323 6b). Pumice fragments are dominant and are mostly aphyric, moderately to high vesicular and range
324 from frothy vesicular to tubular (Fig. 6c), and in some cases exhibit some banding due to the
325 difference in vesicularity. Glass fragments range from dense to poorly vesicular, and typical shapes
326 include blocky, y-shaped and platy. Very rare dark obsidian chips are also present, and a few
327 plagioclases, clinopyroxenes, apatites, biotites ± spinels occur as micro-phenocrysts and in
328 glomeroporphyre. K-feldspars occur as large as 3-4 mm crystals and are rimmed by the vesicular
329 glass; rare quartz crystals also occur. Lithic fragments are extremely rare and consist of altered
330 volcanic rocks (Fig. 6d).
331 Lithostratigraphic unit C (LSU-C, the topmost part of the sequence) is ca. 2 cm-thick in cores TR17-
332 12PC and 11 cm in ANTA02-AV43. The unit comprises coarse-to very fine ash with grey-greenish
333 pumice up to 2 mm in diameter and abundant colorless-light green and rarely honey-yellow glass
334 shards (Figs. 6e-f). As in Unit B, particles forming this unit cover the entire spectrum of shape and
335 vesicularity. Pumice fragments are poorly- to highly-vesicular and range from blocky, frothy
336 vesicular to tubular; some of the pumice fragments contain sparse microcrystals of plagioclase and
337 k-feldspar. Glass shards are abundant and vary from vesicle-free to poorly vesicular, and shapes
338 typically range from blocky, y-shaped to bubble wall. Few accretionary pellets and ash aggregates
339 occur (Fig. 6f). Micro-phenocrysts of k-feldspar, biotite, and clinopyroxene rimmed by the vesicular
340 glass are abundant with some quartz. Lithics occur and consist of altered volcanic rocks and
341 weathered feldspar crystals. In the core TR17-05PC, the AVT tephra is almost entirely represented
342 by the LSU-C. (Fig. 7). Here it is ca. 30 cm-thick, crudely stratified (light and dark bands) and made

of fine ash-sized frothy vesicular to tubular pumice and poorly vesicular to dense glass shards that range from pale-green to honey in color. Sub-millimetric feldspar and mafic crystals occur. Non-volcanic material is scarce and represented by bioclasts (foraminifera, sponge spicule, abundant diatoms).

4.2. Major and trace element volcanic glass compositions

Representative major and trace element volcanic glass compositions of the studied samples are reported in Table 5, and the complete geochemical dataset is reported in Supplementary Material 1. LSU-A of the tephra deposit in cores AV45, AV43 and TR17-12PC shows considerable compositional variation ranging from basanites (44-45 wt.% SiO_2; 1.1-1.2 wt.% $Na_2O + K_2O$) through a dominant component of phonolites and trechytes (59-63 wt.% SiO_2; 13-15.5 wt.% $Na_2O + K_2O$; Fig. 8a). In addition, there is a minor component of more evolved rhyolitic glasses (72-75 wt.% SiO_2; 8.5-11 wt.% $Na_2O + K_2O$; Figs. 8a-b). Owing to the high K_2O content in the glasses they broadly conform to a shoshonitic series (Fig. 8c), and owing to their Na_2O content almost all glasses display low (<1) alkali ratios (Fig. 9d). The exception is the minor component of rhyolitic glasses (cores AV45 and AV43) which fall within the High-K calc-alkaline (HKCA) series and display more elevated alkali ratios (Fig. 9d). The evolutionary trends observed in the glass data indicate that there is a genetic relationship between the basanites, tephrites and trachy-andesites that evolve into phono-trachytes (Figs. 8-9). SiO_2 content can be used as a fractionation index, and whilst it increases the MgO, TiO_2, P_2O_5, CaO (Fig. 9a) and FeO_t (Fig. 9b) contents decrease. In contrast Al_2O_3, K_2O (Fig. 8c), Na_2O (Fig. 9c), Cl contents all increase as SiO_2 content increases. K_2O (Fig. 8c) and Na_2O (Fig. 9c) become lower in the rhyolitic glasses.

Trace element analyses of the volcanic glasses in lithostratigraphic unit A are largely restricted to analyses of the intermediate to silicic components (>54 wt.% SiO_2). The basanites were typically too crystal-rich to yield glassy areas large enough for laser ablation analysis. Consistent with the major

368 elements data, the trace element contents of the glasses are extremely heterogeneous (Fig. 10). For
369 the purposes of describing the trace element data, we outline the chemical signature of the tephrite to
370 trachytic glasses which dominate this lithostratigraphic unit of the tephra deposit and briefly describe
371 the rhyolites separately below. Using increasing Th (6.2-42.1 ppm; Fig. 10) as a fractionation index
372 of the tephrite to phonolites and trachytes glasses we see increasing content of incompatible trace
373 elements including Rb (52-280 ppm), Y (27-139 ppm), Zr (283-1751 ppm), Nb (77-449 ppm), and
374 the Rare Earth Elements (REE; excluding Eu). The volcanic glasses display enrichment in the Light
375 REE (LREE) relative to the Heavy REE (HREE), where La/Yb = 15.2-21.3. Some incompatible trace
376 element ratios remain relatively constant, for instance, Nb/Zr = 0.26 ± 0.03 (2 s.d.), albeit the least
377 evolved glasses display subtly more elevated values, whilst others ratios show considerable
378 variability, for instance, Zr/Th = 36-50. Strontium (707-1 ppm; Fig. 10e), Ba (1455-3 ppm; Fig. 10d)
379 and Eu (5.6-0.8) all behave compatibly with the highest contents observed in the less evolved tephrites
380 and trachy-andesites, and the lowest contents in the more silicic phonolites and trachytes glasses, this
381 is likely to relate to the fractionation of alkali feldspars, observed within the tephra unit. The rhyolitic
382 glasses observed as a minor component within the basal lithostratigraphic unit (A) are enriched in
383 highly incompatible trace elements such as Rb, Th, and U relative to the dominant phono-trachytic
384 glasses and as such follow similar evolutionary trends (Fig. 10). Using Th as the fractionation index,
385 however, reveals that in addition to feldspar-related Sr, Ba, and Eu depletions, the rhyolitic glasses
386 also have lower Zr, Nb, Hf, Ta, and LREE (La-Sm) content relative to the phonolites and trachytes
387 (Fig. 10). Consequently, the LREE in these rhyolitic glasses are less enriched relative to HREE
388 (La/Yb = 9-12) when compared to the dominant phonolites and trachytes.
389 Lithostratigraphic units B and C (TR17-05PC, TR17-12PC, and AV43 cores samples) of the tephra
390 deposit observed in the investigated cores are relatively homogeneous, particularly in relation to basal
391 sub-unit A. Unit B and C glasses are phonolites and trachytes (59.7-63.9 wt. SiO_2; 11.5-15.5 wt.%
392 K_2O + Na_2O) and conform to the shoshonitic series reflected in their K_2O (4.5-5.8 wt.%; Fig. 8c)
393 content, whilst their high-Na (Na_2O = 6.4-10.8 wt.%; Fig. 9c) content is manifested in a LAR

394 (K_2O/Na_2O = 0.4-0.8; Fig. 9d). The phonolites and trachytes glasses overlap entirely with those
395 observed in the basal lithostratigraphic unit (A). Some compositional variability can be observed
396 within these phonolites and trachytes glasses with increasing SiO_2 have lower FeO_t (3.4-7.0 wt.%),
397 MnO, Cl and Na_2O contents, whilst Al_2O_3 (15.8-18.4 wt.%), and K_2O contents increase (Figs. 8-9).
398 CaO and TiO_2 are broadly constant across the SiO_2 range of these phonolites and trachytes glasses.
399 Enrichment in incompatible trace elements contents of these phonolites and trachytes glasses shows
400 considerable range (e.g., 423-1599 ppm Zr; 114-392 ppm Nb; 68-198 ppm La; and 9-37 ppm Th; Fig.
401 10), whilst the incompatible trace element ratios remain constant (e.g., Nb/Zr = 0.26 ± 0.02 [2 s.d.];
402 Zr/Th = 43.8 ± 2.3 [2 s.d.]). The glasses are enriched in LREE relative to the HREE (La/Yb = 16.6 ±
403 1.3 [2 s.d.]).
404
405 **4.3. Geochronology: Constraining the eruption age**

406 Age constraints for cores TR17-05PC (3 levels), TR17-12PC (5 levels), ANTA02-AV43 (2 levels),
407 and ANTA02-AV45 (1 level) are based on new calibrated AMS ^{14}C dates. Meanwhile, two
408 radiocarbon dates from Colizza et al. (2004) and another one from Mezgec et al. (2017) were used
409 and re-calibrated for ANTA02-AV45 core and BAY05-bc40 box core (Table 2).
410 The age obtained at 98-99 cm core-depth in TR17-05PC, is the only one produced for sediments
411 under the tephra. This age was determined in a diamicton sequence just at the bottom of the tephra
412 and is 17.7 ± 0.3 cal ka BP. On the contrary, we have much information about the age of sediments
413 located above of the tephra layer (Fig. 2). These span between 9.38 ± 0.2 cal ka BP in core ANTA02-
414 AV43, to 5.6 ± 0.2 cal ka BP in core TR17-05PC and are stratigraphically compatible with the age of
415 the underlying tephra (see below). The difference of about 4 ka that exists in these ages may be the
416 result of several processes that affected the area. In cores sampled closer to the edge of Aviator Glacier
417 (ANTA02-AV43, ANTA02-AV45 and TR17-12PC), a slight difference in the detrital sediments
418 input from the glacier could have occurred in the three core sites. Consequently, different
419 sedimentation rates for the three sequences could explain the difference of ca. 1.7 ka in the age of

sediments sampled on top of the tephra. Conversely, in core TR17-05PC, which is located more offshore and less influenced by detrital input from Aviator Glacier the young age of 5.6 ± 0.2 cal ka BP obtained above the tephra cannot be explained by variation in detrital sediment input from the Aviator Glacier. Vice versa, we suggest that a sedimentary hiatus or a strong decrease in the sedimentation rate could have occurred after the deposition of the tephra layer. No sedimentary structure indicates the presence of a any sedimentary hiatus thus this first hypothesis must be rejected. We suggest that during the early Holocene the area where core TR17-05PC is located was ice covered, but close to the ice shelf edge, except in the period of the tephra deposition. This caused very-low sedimentation rates. The marine sedimentation could have started again, with a sedimentation rate consistent with the coastal cores, around 5.6 cal ka BP in agreement with Mezgec et al. (2017), who indicated the beginning of the open marine sedimentation in the central Aviator Basin at approximately 5.7 ± 0.2 ka BP. Therefore, according to AMS ^{14}C date the AVT tephra could be temporally placed between approximately 18 and 6 cal ka BP.

^{40}Ar-^{39}Ar ages were obtained on alkali-feldspar crystals extracted from the tephra between 404-414 cm b.s.f. in LSU-B of the core TR17-12PC. Eighteen total fusion analyses of single alkali-feldspar grains gave ^{40}Ar-^{39}Ar ages in the range of 7.6 ± 3.9 ka to 280 ± 7 ka. In a cumulative probability plot (Fig. 12), the data reveal a dominant younger peak defined by nine data points and yielding a mean age of 11.1 ± 1.4 ka (MSWD = 1.33), with minor peaks at 18, 27, 53 and 280 ka. Three step-heating runs were performed on a multigrain fraction and two single grains (see Table 3). The multigrain fraction yielded a discordant age profile with a total gas age of 18 ± 10 ka. Two concordant and consecutive steps, representing >50% of the total $^{39}Ar_K$ released, yield a mean age of 12.3 ± 2.4 ka. One single grain gave a descending profile, with the final step (representing >65% of the total $^{39}Ar_K$ released) yielding an age of 13.6 ± 2.2 ka. The second gave a concordant age profile yielding an age of 20.1 ± 4.1 ka. Comparable ages were previously reported by Del Carlo et al. (2015), who recovered a total of 38 alkali-feldspar grains (~27 mg) from a tephra layer found in the core ANTA02-AV43, at sediment depth of 138-139 cm (Fig. 12). Feldspar grains were split into five aliquots based on their

morphology and analyzed by the ^{40}Ar-^{39}Ar method through an older generation single-collector noble gas mass spectrometer. In a cumulative probability plot, age data match remarkably those obtained for the core TR17-12PC from the present work, although data by Del Carlo et al. (2015) are much less precise and performed on multigrain fractions. Indeed, data by Del Carlo et al. (2015) define a distinct peak (n = 3) yielding an error-weighted mean of 9.7 ± 5.3 ka, and single data points define small peaks at ~170 ka and 280 ka. One analysis performed on a single grain gave a very poorly defined age of 21 ± 17 ka. These data, given they were completed on multigrain fractions, were conservatively interpreted to define an eruption age of the tephra of ≤12 ka. Independent tephra age determinations were not possible for the tephra layers in cores ANTA-AV45 and TR17-05PC. This was due to the overall small size of feldspar crystals thus non-suitable for ^{40}Ar-^{39}Ar dating. The time range of the tephra deposition, proposed by ^{40}Ar-^{39}Ar ages seems to be consistent with the radiocarbon dates. As a whole, the most reliable age for AVT tephra is therefore 11.1 ± 1.4 ka.

4.4. Diatoms

In the studied levels of core TR17-12PC (357-406 cm), diatoms are abundant and not reworked (Table 4). The absolute diatom abundances varies from 49.0 to 790.9 x 10^6 nv/gds. It reaches a maximum value at the end of the tephra interval (397.5 cm). The diatom assemblage is dominated by *Fragilariopsis curta* (18.4-36.3%) and *Thalassiosira antarctica* (23.2-37.2%). These species have a push-pull trend. *Eucampia antarctica* is rare (< 2%) except for the level at 382.5 cm, where it reaches the abundance of 13.5%. In the studied level of core TR17-05PC (38.5-107.5 cm), the absolute diatom abundances varies from 2.6 to 2620.8 x 10^6 nv/gds with the highest abundances observed toward the top of the studied interval. The assemblages are dominated by *Fragilariopsis curta* (14.3-63.5%), and subordinate *Thalassiosira antarctica* (0.0-42.86%); they have an opposite trend. Also in this core *Eucampia antarctica* is rare, and it occurs in two peaks: the first at 90.5 cm and the second at 72.5 cm, that comprise 16.7% and 13.2% of the assemblage, respectively. In the core ANTA-AV45 (data discussed in Colizza et al., 2004) the assemblages are dominated by *T. antarctica* (> 20%) between

160 and 100 cm, and by *F. curta* from 100 cm toward the top (Colizza et al., 2004); they have an opposite trend, as previously observed. Indeed, *E. antarctica* becomes dominant in a laminated layer (70-55 cm) and at the same level, the abundance of *F. curta* abruptly decreases.

5. Discussion

5.1. The origin of the Aviator Tephra (AVT)

Tephra layers identified have been easily correlated in the studied cores based on stratigraphic relationship, lithologic characteristics, and geochemical composition (Figs. 2-11). To determine the volcanic source of the AVT the geochemical composition of the tephra was compared with major- and trace-element compositions of Neogene-Quaternary tephra layers from Antarctic ice cores, marine sediments, blue ice and continental outcrops in Antarctica and circum-Antarctic areas contained in AntT database (http://www.tephrochronology.org/AntT/database.html) and in Del Carlo et al. (2018). Considering the thickness of the tephra and the coarse grain size, we have focused our research on those volcanoes that are relatively close (<200 km) to the coring site and were active during the Late Pleistocene and Holocene. The volcanoes considered as the possible source are Mount Melbourne, Mount Rittmann and The Pleiades volcanic complexes in the Northern Victoria Land, situated approximately 50-60 km, 75-90 km and 175-200 km from the coring sites, respectively. We also included the Erebus volcano which is located further to the south (ca. 370 km) because it was very active during the relevant time period as testified by the number of englacial tephra layers found on the flank of Ross Island (Harpel et al., 2008). Unfortunately, only a limited major and trace element volcanic glass data are available in the literature for the proximal pyroclastic deposits of the above-mentioned volcanoes (Erebus excluded), and these data are critical to accurately provenancing marine tephra deposits. Major element glass data are more widely available for tephra of the Northern Victoria Land volcanoes preserved in englacial medial settings (blue ice fields). Major element glass data are also available for eruption deposits preserved in regional ice cores which are thought to relate

497 to these volcanoes. Available reference glass data are exclusively related to evolved products of the
498 above-mentioned volcanoes (phonolites and trachytes), and as such our provenancing centers on the
499 clearly juvenile phonolites and trachytes magma compositions that are dominant within the distal
500 AVT eruption deposit.
501 The most distal volcanic source considered here for the AVT, Erebus, can be easily excluded based
502 on available glass datasets. Erebus's silicic products are restricted to lower-SiO_2 phonolitic glasses,
503 which are very different from the dominant higher-SiO_2 phonolites and trachytes glasses of the AVT
504 (Fig. 8). These phonolitic Erebus glasses exhibit noticeably higher Al_2O_3 (ca. 19-20 wt.%) and CaO
505 (ca. 2 wt.%) contents relative to the phonolites and trachytes glasses of the AVT (Table 5). Major and
506 trace element glass compositions, specifically those of the phonolites and trachytes component of the
507 AVT (and its mineral assemblage) are extremely consistent with the phono-trachytic pumices and
508 breccias found at Mount Rittmann caldera rim (Armienti and Tripodo, 1991; Di Roberto et al., 2019;
509 Lee et al., 2019; Figs. 8-10), and can be clearly distinguished from the products of other silicic
510 volcanism from Mount Melbourne and The Pleiades. Based on the limited major element data
511 available for Mount Melbourne and The Pleiades, it is clear that their evolved glasses are offset to
512 higher SiO_2 content and noticeably lower Na_2O contents relative those of AVT and Mount Rittmann,
513 which is manifested in their lower alkali ratio (Fig. 9d). These interpretations are further corroborated
514 by statistical analysis of the geochemical data, where the SC value of 0.94 and D^2 values of 3.25-4
515 are determined between the phonolites and trachytes glass composition of the AVT (considered as
516 the juvenile magma composition) and Mount Rittmann pyroclasts. Overall, the chemical evidence
517 linking the AVT to explosive products and activity at Mount Rittmann is compelling.
518 There is geochemical similarity between the AVT and three marine tephra (SC = 0.90-0.93 and D^2 =
519 5.7-9.5) found interbedded in Holocene-Late Pleistocene marine sediments in cores recovered from
520 the Drygalski basin, in western Ross Sea (Del Carlo et al., 2015; Fig. 11). Whilst these eruption
521 deposits were initially linked to Mount Melbourne, they have been recently attributed to explosive
522 volcanism of Mount Rittmann on the basis of near-source geochemical data (Lee et al., 2019). Two

of the tephra layers have been correlated between cores based on their shared glass chemical signature and indistinguishable ^{40}Ar-^{39}Ar ages of 23.7 ± 5.3 ka (ANTA02-NW2-0-13) and 21.2 ± 6.4 ka (ANTA02-NW31-42-61). A third tephra layer (ANTA02-NW2-255-265) from the same core set, also shares a Rittmann-like glass composition (SC=0.93 and D^2 =1.94), consistent with the two above mentioned marine tephra layers, but this tephra has a deposition age based on ^{40}Ar-^{39}Ar data of 74.6 ± 2.1 ka (Del Carlo et al., 2015; Fig. 11).

There is also a very close compositional similarity between the AVT and the much more recent, historic Mount Rittmann tephra conventionally referred to as the 1254 C.E. (or 1252 ± 2) tephra (SC = 0.98 and D^2 = 1.2) found in ice cores at Taylor Dome (Dunbar et al., 2003b), Siple Dome (Dunbar and Kurbatov, 2011) and Talos Dome (Narcisi et al., 2010; 2012), in several shallow ice cores in East and West Antarctica (Styx Glacier, RICE, WDC05, and WDC06A; Lee et al., 2019; Sigl et al., 2016) at two blue ice areas (Brimstone and Rennick blue ice areas; Lee et al. 2019), and in marine sediments of Cape Hallett (Di Roberto et al., 2019; Tesi et al., 2020). Finally, remarkable similarity also occurs between the tephra layers studied here and several tephra layers found in ice cores from Talos Dome, Siple Dome and RICE ice cores (Supplemental Material 3) spanning the last c. 65 ka. In particular high values for the statistical correlation coefficients exist with tephra layers TD741 (SC = 0.98 and D^2 = 0.53), and TD779 (SC = 0.92 and D^2 = 3.54) dated at 13.77 ± 0.13 ka and 15.36 ± 0.38 ka, respectively and previously correlated, with the volcanic activity of the Melbourne volcanic province and/or from the Pleiades (Narcisi et al., 2012; Fig. 11). The TD779 tephra was also correlated with tephra SDMA-9053 in the Siple Dome ice core, which in turn is dated at ca. 15.3 ka (Dunbar and Kurbatov, 2011; Fig. 11).

Geochemical evidence indicates that Mount Rittmann is not only the most likely source of the Early-Holocene AVT tephra described here, but also the source of several tephra layers found in regional marine sediments and continental ice-archives. Integrating the various distal occurrences of Mount Rittmann ash fall deposits, including the AVT, provides critical insights into the eruptive history of the volcano, which until now had remained poorly known, largely owing to limited near-source

549 preservation of the eruption record. According to studied marine sequences, the explosive activity of
550 Mount Rittmann can be traced back to 74 ka with at least four explosive events of considerable
551 magnitude recognized. Each of these events deposited centimeter-thick, relatively coarse, pyroclastic
552 fallout at distances of several tens to thousands of kilometers from the source
553
554 **5.2. Implications for eruptive style**

555 The analysis of tephra layers from many different sedimentary environments indicates that tephra
556 from fine, deep-sea sediment sequences provide useful information on eruption processes and tephra
557 dispersal (Engwell et al., 2014). This is true especially when tephra fallout is rapidly transferred to
558 the seafloor and not affected by strong bioturbation, remobilization, or reworking processes (McCoy,
559 1981). The AVT shows key primary features, such as a sharp basal contact with the underlying
560 glaciomarine sediments, a gradational upper contact that transitions into the overlying sediment, well-
561 defined stratification, low concentration of detrital material and bioclasts, good sorting (at least the
562 unit interpreted as Plinian fallout), and the broadly homogeneous geochemical phono-trachytic glass
563 compositions. Despite strong ocean currents in the region, these features unequivocally indicate that
564 the AVT deposits are not ice-rafted, and have not been significantly remobilized prior to final
565 deposition in the Aviator Basin.
566 On this basis, vertical variation recorded in studied tephra sequences is interpreted in terms of changes
567 in the fragmentation mechanisms, eruptive style and dynamics, and sedimentation processes (Fig.
568 13).
569 Deposits of LSU-A comprise very fine, poorly-sorted ash and abundant accretionary pellets and ash
570 aggregates (Fig. 5). These two features are commonly interpreted as diagnostic of elevated magma
571 fragmentation efficiency during magma-water interaction in explosive eruptions (Self, 1983; Self and
572 Sparks, 1978; Sheridan and Wohletz, 1983; Walker, 1981). In a glacial setting, the interactions
573 between magma and water (meltwater) may have resulted in highly explosive hydromagmatic activity
574 with enhanced ash production (Gudmundsson et al., 1997; Smellie and Skilling, 1994; Stevenson et

575 al. 2011; Tuffen, 2010). The abundance of complex-structured accretionary pellets and ash aggregates
576 is also indicative of specific eruptive mechanisms. Particle aggregates and accretionary pellets can be
577 found in deposits from a range of explosive volcanic eruptions and are very common in
578 hydromagmatic eruptions (Brown et al., 2010; Gilbert and Lane, 1994; Moore and Peck, 1962; Self
579 and Sparks, 1978). Broadly, particle aggregates may form either by the adhering of particles or by
580 the progressive accretion of layers made by fine-grained particles to a larger clast acting as a core
581 (Brown et al., 2010) and has been interpreted as the result of electrostatic attraction between ash
582 particles, moist adhesion (Brown et al., 2010; Gilbert and Lane, 1994; James et al., 2003; Schumacher
583 and Schmincke, 1995, 1991), and ice riming (Textor et al., 2006; Veitch and Woods, 2001). Resulting
584 aggregates display a wide range of internal texture which reflects different mechanisms and dynamics
585 of aggregations and in turn different eruption dynamics and depositional processes. In the studied
586 deposits the presence of almost all known types of accretionary pellets and ash aggregates suggests
587 that these formed by different accretion mechanisms and evolved by moving through different regions
588 of the eruptive column. Preserved aggregate particles are pertinent either to subaerial or shallow water
589 deposits (Murtagh and White, 2013; Van Eaton and Wilson, 2013) and with the exception of a few
590 cases (Boulter, 1987; White, 1996), they are thought to unlikely survive to deposition in distal sites
591 and in deep-water deposits (Russell et al., 2013; Van Eaton and Wilson, 2013). The ash aggregates
592 and accretionary pellets in the studied deposits have been perfectly preserved in the marine
593 environment in water depthsup to 1000 m which means that they were already indurated-cemented
594 when settled through the water column. This, in turn, indicates that they have long resided inside a
595 sustained eruptive plume allowing the cementation of particles; alternatively, also considering the
596 climatic condition of the Antarctic environment, a possibility is that aggregates were frozen in the
597 eruptive column and remained in the same condition until the final deposition and successive
598 diagenesis.
599 LSU-B, which comprise well-sorted pumiceous ash and fine lapilli (Fig. 6), marks the sharp transition
600 to different fragmentation and eruptive mechanisms. The transition was probably controlled by a

change in magma discharge rate and/or magma/water mixing ratio i.e. the magma discharge was too high to maintain extensive melt-water interaction and the production of highly fragmented material (Liu et al., 2017) or that water was drained from the vent site. As a consequence, a sustained Plinian column likely rose into the atmosphere and pumice lapilli was transported by prevailing winds to more than 80 km from the vent (Fig. 13c).

The massive and crudely stratified, ash-rich LSU-C (Figs. 6g-h), might be the result of renewed efficient magma-water interaction, perhaps due to a significant drop in the magma eruption rate or to other external factors. This layer may have been emplaced by dilute ash-rich co-ignimbrite plumes accompanying pyroclastic density currents (Fig. 13d). The presence of a polymictic unwelded lag breccia around the rims of the Mount Rittmann caldera (Armienti and Tripodo, 1991) indicates there were substantial pyroclastic density currents (PDC), and LSU-C could be the co-ignimbrite fallout associated with these. The PDCs include juvenile pumice (samples NN13 and NN15 of Armienti and Tripodo, 1991), with the same geochemical and mineralogical composition of the studied tephra, and the deposit were attributed by Armienti and Tripodo (1991) to the last large explosive eruption of the Mount Rittmann volcano. Co-ignimbrite ash-fall deposits were possibly dispersed with a more eastern-directed axis with respect to fallout deposits of LSU-B and potentially influenced by strong low-altitude winds that are common in this region. This seems confirmed by the reduced thickness of this layer in ANTA02-AV43 and TR17-12PC cores located closer to the coasts (75 km and 77 km from the vent), and conversely the higher thickness in core TR17-05PC (100 km from the vent).

In conclusion, LSU-A, B, and C in described for core ANTA02-AV43, ANTA02-AV45, TR17-12PC, and TR17-05PC record multiple eruptive phases (Fig. 13), of a highly-explosive, high-magnitude, possibly caldera-forming eruption, fed by a broadly homogeneous phonolitic-trachytic magma and sourced in Mount Rittmann.

The presence of glass compositions ranging from basaltic to phonolitic-trachytic coexisting in the LSU-A indicates that at least two magmas were involved in the eruptions. Furthermore, subtle variability observed within the juvenile phonolites and trachytes glasses may indicate that discrete

627 silicic magma batches were tapped during this large-magnitude eruption (see a similar scenario in the
628 Monte Epomeo Green Tuff eruption at Ischia; Tomlinson et al., 2014), for instance subtly distinct
629 phonolitic populations can be distinguished by their lower SiO_2 and CaO contents, and higher Na_2O
630 content relative to the more dominant phonolites and trachytes glasses (Figs. 8-9). In terms of
631 explaining the genetic relation between basalts through basaltic trachy-andesite to trachy-andesites a
632 selection of different explanations can be proposed. Firstly, these melts compositions represent
633 injections of a deep, hot, gas-rich mafic end-member and the transfer of heat into a more silicic
634 magma (phonolites and trachytes) residing at a shallower lithospheric depth, a common triggering
635 mechanism for large explosive eruptions (Morgavi et al., 2019; Murphy et al., 1998, 2000). Here, the
636 scarcity of intermediate glass compositions or mingled products would suggest only a limited
637 interaction between the two magmas. An alternative scenario is that a phonolites and trachytes magma
638 could have ascended and intersected a small basaltic magma body (sill/dike) and as a result of the
639 incoming magma, the mafic melts would have pushed to the surface through a fracture system and
640 ejected during the first phases of the eruption. The eruption then continued with the emission of
641 homogeneous and gas-rich phono-trachytic magma. Similar mechanisms are proposed for other
642 bimodal eruptions characterized by reverse zoning, such as the Lower Pollara eruption of Salina, Italy
643 (Calanchi et al., 1993) or for the Monte Guardia eruption of Lipari, Italy (De Rosa et al., 2003).
644 Finally, the fragments analysed with basaltic to intermediate compositions could be cognate lithics
645 deriving from previous eruptions of Mount Rittmann and expelled during the initial phases of the
646 eruption. This final explanation is certainly the most likely reason for the minor components of highly
647 evolved rhyolitic material observed in lithostratigraphic unit A of the AVT in core ANTA02-AV43
648 and ANTA02-AV45.
649
650 5.3. **Paleoenvironmental significance of Aviator Tephra**
651 In polar regions, pyroclastic deposits resulting from the explosive subaerial volcanic activity may be
652 emplaced on ice-shelves, sea ice, or directly in open waters depending on the environmental

conditions at the time of tephra deposition. Deposition on ice surfaces, transport due to ice rafting, and consequent redeposition/redistribution processes after ice melting have a major impact on the integrity of tephra stratigraphy and structure. Several studies have focused on the preservation of tephra in glaciomarine marine sediment sequences especially in the northern hemisphere, to determine primary depositional features (Abbott et al., 2011, 2013; Griggs et al., 2014). By backward reasoning, the degree of preservation of primary stratigraphy and structures in marine tephra layers can be then used to constrain the paleoenvironmental conditions at the time of tephra emplacement (Van Der Bilt and Lane, 2019). In our study area, the preservation of the primary stratigraphy and the structures of the studied tephra suggests that Wood Bay was probably open water during the early Holocene. If at the time of the deposition even thin sea ice was present in the Wood Bay area, the deposits would have first been deposited on the ice, and once the ice melted they would have sunk through the water column. Such multi-stage deposition would have resulted in a chaotic deposit without complex stratification.

Diatom assemblages in the sediments located immediately above the tephra layers (our data and Colizza et al., 2004) contain *Fragilariopsis curta* that reflect seasonal sea ice and/or the very close presence of an ice shelf margin (i.e. Alley et al., 2018; Armand et al., 2005)). In addition, the co-presence of *Talassiosira antarctica*, less abundant than *F. curta*, suggests cold sea surface temperatures and open water conditions (Cunningham et al., 1999; Leventer, 2011) and/or unconsolidated sea ice presence (Armand et al., 2005; Leventer et al., 1996; Pike et al., 2009). These diatom data indicate open water conditions in the coastal area of the Wood Bay by about 11 ka BP (tephra ages), which presumably started during the global meltwater pulse (MWP) 1B, dated 12-10 ka BP for the Southern Ocean (Golledge et al., 2014; Lowry et al., 2019) and are in agreement with the deglacial history of the area. In the western Ross Sea, the retreat of the ice sheet from the continental shelf occurred by 13 cal ka BP (Anderson et al., 2014) and the calving front passed over the Drygalski Trough at 74°S by 9.5 ka BP (Domack et al., 1999). These conditions of open water, with only seasonal sea ice, permitted the deposition of the AVT tephra.

679

680 ## 6. Conclusions

681 We report on the identification of a thick tephra layer (AVT tephra) in the marine sediment record
682 from the Aviator Basin, Ross Sea, Antarctica. We examined tephra deposit stratigraphy,
683 componentry, and texture which all imply that it was produced by a large-magnitude explosive
684 eruption. The major and trace element compositions of the glass shards allow us to correlate the tephra
685 with Mount Rittman volcano, in the Northern Victoria Land. ^{40}Ar-^{39}Ar age determinations on alkali-
686 feldspar crystals indicate that the eruption occurred at ~11 ka, which is confirmed by ^{14}C ages, which
687 age is supported by ^{14}C dates from sediments overlying the tephra. The marine tephra deposits provide
688 insights into the eruption dynamics; the eruption began with an intense and prolonged phase in which
689 the hydromagmatic activity was dominant, favoring the production of fine ash and the formation of
690 ash aggregates and accretionary pellets. The climatic phase of the eruption coincides with the
691 transition to a purely magmatic activity. This phase of the eruption deposited ash and pumiceous
692 lapilli from a high, sustained Plinian column. The eruption then moved into the final phase,
693 characterized by the deposition of a thick, stratified layers of fine ash with few aggregates. This could
694 be linked to co-ignimbrite ash associated with PDCs generated during the collapse of the eruptive
695 column. Presently, the AVT tephra unequivocally presents the evidence for a large-magnitude,
696 possibly caldera-forming, Early-Holocene eruption in northern Victoria Land.

697 The AVT also constitutes a potential marker for time-stratigraphic correlation between marine
698 archives of the Ross Sea and facilitation for the synchronization of these with continental ice-archives.
699 Such correlations are pivotal to integrate data derived from different earth climatic systems and
700 understanding their connections.

701 Additionally, from the perspective of paleoenvironmental reconstruction, the primary features of the
702 tephra and diatom types indicate that the tephra was deposited during at least relatively open water
703 conditions in the Wood Bay.

704

Acknowledgments

This work has been funded by TRACERS Project (PNRA16_00055 - A3). G.D.V. is indebted to P.R. Renne, who kindly provided the fluence monitor Alder Creek sanidine. P.G.A. is funded through a UKRI Future Leaders Fellowship (MR/S035478/1). B.S. benefited of a research fellowship in the framework of TRACERS Project (PNRA16_00055 - A3).

The Authors Gratefully Acknowledge Professor J. Smellie and an anonymous referee that provided valuable comments and suggestions that helped to improve the manuscript. Many thanks to Quaternary Science Reviews Editor Giovanni Zanchetta for the editorial handling of our work.

Figures

Figure 1. Bathymetric map with locations of ANTA02-AV43, ANTA02-AV45, TR17-05 PC and TR17-12 PC cores. Bathymetry data from Arndt et al. (2013). The red dashed line roughly highlights the Aviator Basin and orange triangle show main volcanic complexes proximal to the coring sites. Inlet: schematic representation of volcanic rock outcrops from the McMurdo volcanic group (grey fields) including the Melbourne volcanic province of northern Victoria Land and Erebus volcanic province of the southern Victoria Land. Tectonics of this region are also schematically reported (redrawn from Kyle, 1990)

Figure 2. Stratigraphic logs of ANTA02-AV43, ANTA02-AV45, TR17-05 PC and TR17-12 PC cores with highlighted in red the studied tephra layers. ^{14}C (red lines this work and green lines from Colizza et al. 2003) and ^{40}Ar-^{39}Ar (blue lines this work; yellow line Del Carlo et al. 2015) dated horizons are also reported.

Figure 3. a) Photograph and x-ray images of ANTA02-AV43-I, ANTA02-AV45-II, TR17-05 PC-III and TR17-12 PC-I cores sections with highlighted the AVT tephra (red bar).

Figure 4. a) Photograph of the TR17-12 PC-I core section (318-416.5 cm core depth) and detail of the AVT tephra. b) close up of AVT tephra with highlighted the lithostratigraphic units (LSU) A, B, and C (409-416.5 cm core depth).

Figure 5. Table of photographs taken at various magnifications by stereomicroscope (a-b) and scanning electron microscope (SEM; g-h) showing the texture of accretionary pellets and ash aggregates found in AVT from ANTA02-AV43, ANTA02-AV45 and TR17-12PC cores. A-b) stereomicroscope and (c-d) SEM images of accretionary pellets and ash aggregates representing the main part of Litostratigraphic Unit A (LSU-A). E) Ash aggregates formed by multiple concentric layers of very fine ash around a magmatic crystal similar to AP2-type aggregates described by Brown et al. (2012). F-g) Mostly unstructured to poorly structured ash aggregates (AP1-type aggregates of Brown et al. (2012), and h) aggregated formed by a cluster of few microns-sized AP1 and AP2 type aggregates.

Figure 6. Table of photographs taken by stereomicroscope and scanning electron microscope showing the texture of volcanic fragments forming the AVT in ANTA02-AV43, ANTA02-AV45 and TR17-05PC and TR17-12PC cores. A-b) Stereomicroscope image of pumiceous lapilli and glass shards fragments forming Litostratigraphic Unit B (LSU-B). C-d) SEM backscatter images of aphyric, moderately to high-vesicular pumices and K-feldspars crystals rimmed by the vesicular glass. E-f) SEM backscatter images showing variably vesicular glass fragments, microcrystals, rare accretionary pellets and ash aggregates, and lithic fragments (altered volcanic rocks and weathered feldspar) forming Litostratigraphic Unit C (LSU-C).

Figure 7. a) Photograph of the TR17-05 PC-III core section (38-134 cm core depth) and b) detail of the fine-grained LSU-C (62.5-90.5 cm core depth).

752 Figure 8. Major element glass geochemical variation of the collectively known Aviator Tephra,
753 preserved in marine sediment cores TR-17-12PC, TR17-05PC, ANTA02-AV43 and ANTA02-AV45,
754 and compared to volcanic glasses of explosive eruption deposits produced by Mount Rittmann (Di
755 Roberto et al., 2019; Lee et al., 2019), The Pleiades (Lee et al., 2019), Mount Melbourne (Lee et al.,
756 2019), and Erebus volcano (Harpel et al., 2008). a) TAS classification diagram of AVT volcanic a;
757 b) a TAS classification diagram of dominant phonolites and trachytes juvenile component of the
758 AVT; c) SiO_2 vs K_2O classification diagram. Error bars represented 2 standard deviations of
759 replicated analyses of the MPI-DING StHs6/80-G secondary standard glass run alongside the marine
760 tephra samples.

761 Figure 9. Major element Harker diagrams showing the geochemical variation of the AVT (cores TR-
762 17-12PC, TR17-05PC, ANTA02-AV43 and ANTA02-AV45) volcanic glasses compared to those of
763 proximal deposits of the Northern Victoria Land volcanoes, Mount Rittmann (Di Roberto et al., 2019;
764 Lee et al., 2019), The Pleiades (Lee et al., 2019) and Mount Melbourne (Lee et al., 2019). Error bars
765 represented 2 standard deviations of replicated analyses of the MPI-DING StHs6/80-G secondary
766 standard glass run alongside the marine tephra samples.

767 Figure 10. Trace element variation diagrams of the volcanic glasses within the AVT (cores TR-17-
768 12PC, TR17-05PC, ANTA02-AV43 and ANTA02-AV45) compared to the trachytes of Mount
769 Rittmann sampled from the caldera rim (Di Roberto et al., 2019; Lee et al., 2019).

770 Figure 11. Major element variation diagrams illustrating the similarity between the juvenile phono-
771 trachytic AVT deposits and average compositions of other phonolites and trachytes distal tephra
772 deposits reported from the marine sediments of the Ross Sea, and various Antarctic continental ice
773 records which are all linked to activity at Mount Rittmann (See text for the data source reference;
774 error bars represent 1 standard deviation of the data average).

775 Figure 12. Cumulative probability a) and ranked distribution b) of ^{40}Ar-^{39}Ar ages from total fusion
776 experiments on alkali feldspar of AVT tephra recovered in the core TR17-12PC. Data are compared

777 with those obtained by Del Carlo et al. (2015) found in the core ANTA02-AV43, at sediment depth
778 of 138-139. Note that data from this work have been completed by a new generation of multicollector
779 mass spectrometers (ARGUS VI). Cumulative probability distributions were calculated using v. 3.75
780 of the Isoplot/Ex program (Ludwig, 2012).

781 Figure 13. Sketch showing a possible reconstruction of the eruptive phases of the AVT eruption. a)
782 Rittmann edifice before the onset of the eruption. b) The onset of the eruption with intense
783 hydromagmatic activity and the formation of accretionary pellets and ash aggregates. c) Plinian
784 climax phase. d) PDC-dominated phase with associated co-ignimbrite plumes over the top of the
785 PDCs during renewed hydromagmatic activity. Eruption columns and PDCs are not to scale.

786 Table 1.Locations of cores used in this study with coordinates, sampling water depths, and core
787 lengths. Tephra thickness and Litostratigraphic Units (LSU) intervals are also reported.

788 Table 2. AMS ^{14}C ages with calibrated calendar ages $\pm 1\sigma$ (yr) and applied local contamination offset
789 and reservoir age correction (see text) for cores ANTA02-AV43, ANTA02-AV45, TR17-5PC, TR17-
790 12PC and box cores BAY05-bc40 and TR1705bc.

791 Table 3. ^{40}Ar-^{39}Ar data on alkali feldspars of tephra TR17-12 PC.

792 Table 4. Diatom relative abundances of *Eucampia antarctica*, *Fragilariopsis curta* and *Thalassiosira*
793 *antarctica* and ADA (absolute diatom abundances) in the level close to tephra in cores TR17-12PC
794 and TR17-05P.

795 Table 5. Representative glass analyses of the AVT marine tephra deposits identified in cores from the
796 Aviator basin.

797

798 **References**

799 Abbott, P.M., Austin, W.E.N., Davies, S.M., Pearce, N.J.G., Hibbert, F.D., 2013.

Cryptotephrochronology of the Eemian and the last interglacial-glacial transition in the North East Atlantic. J. Quat. Sci. 28, 501-514. https://doi.org/10.1002/jqs.2641

Abbott, P.M., Davies, S.M., Austin, W.E.N., Pearce, N.J.G., Hibbert, F.D., 2011. Identification of cryptotephra horizons in a North East Atlantic marine record spanning marine isotope stages 4 and 5a (~60,000-82,000 a b2k). Quat. Int. 246, 177-189. https://doi.org/10.1016/j.quaint.2011.07.033

Adamson, R.G., Cavaney, R.J., 1967. Volcanic Debris-Layers Near Mount Melbourne, Northern Victoria Land, Antarctica. 10, 418-421. New Zeal. J. Geol. Geophys. https://doi.org/10.1080/00288306.1967.10426745

Alley, K., Patacca, K., Pike, J., Dunbar, R., Leventer, A., 2018. Iceberg Alley, East Antarctic Margin: Continuously laminated diatomaceous sediments from the late Holocene. Mar. Micropaleontol. 140, 56-68. https://doi.org/10.1016/j.marmicro.2017.12.002

Anderson, J.B., Conway, H., Bart, P.J., Witus, A.E., Greenwood, S.L., McKay, R.M., Hall, B.L., Ackert, R.P., Licht, K., Jakobsson, M., Stone, J.O., 2014. Ross Sea paleo-ice sheet drainage and deglacial history during and since the LGM. Quat. Sci. Rev. 100, 31-54. https://doi.org/10.1016/j.quascirev.2013.08.020

Andrews, J.T., Domack, E.W., Cunningham, W.L., Leventer, A., Licht, K.J., Jull, A.J.T., DeMaster, D.J., Jennings, A.E., 1999. Problems and possible solutions concerning radiocarbon dating of surface marine sediments, Ross Sea, Antarctica. Quat. Res. 52, 206-216. https://doi.org/10.1006/qres.1999.2047

Antoniades, D., Giralt, S., Geyer, A., Álvarez-Valero, A.M., Pla-Rabes, S., Granados, I., Liu, E.J., Toro, M., Smellie, J.L., Oliva, M., 2018. The timing and widespread effects of the largest Holocene volcanic eruption in Antarctica. Sci. Rep. 8(1). https://doi.org/10.1038/s41598-018-35460-x

824 Armand, L., 1997. The use of diatom transfer functions in estimating sea-surface temperature and
825 sea-ice in cores from the southeast Indian Ocean. Australian National University, Canberra,
826 Thesis (PhD). https://doi.org/10.25911/5d6513d00b7b5

827 Armand, L.K., Crosta, X., Romero, O., Pichon, J.J., 2005. The biogeography of major diatom taxa
828 in Southern Ocean sediments: 1. Sea ice related species. Palaeogeogr. Palaeoclimatol.
829 Palaeoecol. 223, 93-126. https://doi.org/10.1016/j.palaeo.2005.02.015

830 Armienti, P., Tripodo, A., 1991. Petrography and chemistry of lavas and comagmatic xenoliths of
831 Mt. Rittmann, a volcano discovered during the IV Italian expedition in Northern Victoria Land
832 (Antarctica). Mem. della Soc. Geol. Ital. 46, 427–451.

833 Arndt, J.E., Schenke, H.W., Jakobsson, M., Nitsche, F.O., Buys, G., Goleby, B., Rebesco, M.,
834 Bohoyo, F., Hong, J., Black, J., Greku, R., Udintsev, G., Barrios, F., Reynoso-Peralta, W.,
835 Taisei, M., Wigley, R., 2013. The International Bathymetric Chart of the Southern Ocean
836 (IBCSO) Version 1.0 - A new bathymetric compilation covering circum-Antarctic waters. 40,
837 3111-3117. https://doi.org/10.1002/grl.50413

838 Bonaccorso, A., Maione, M., Pertusati, C., Privitera, E., Ricci, C.A., 1991. Fumarolic activity at
839 Mount Rittmann volcano (northern Victoria Land, Antarctica). Mem. della Soc. Geol. Ital. 46,
840 453–546.

841 Boulter, C.A., 1987. Subaqueous deposition of accretionary lapilli: Significance for
842 palaeoenvironmental interpretations in Archaean greenstone belts. Precambrian Res. 34, 231-
843 246. https://doi.org/10.1016/0301-9268(87)90002-7

844 Brown, R.J., Bonadonna, C., Durant, A.J., 2012. A review of volcanic ash aggregation. 45-46, 65-
845 78. Phys. Chem. Earth. https://doi.org/10.1016/j.pce.2011.11.001

846 Brown, R.J., Branney, M.J., Maher, C., Dávila-Harris, P., 2010. Origin of accretionary lapilli within
847 ground-hugging density currents: Evidence from pyroclastic couplets on Tenerife. Bull. Geol.

848 Soc. Am. 122, 305-320. https://doi.org/10.1130/B26449.1

849 Burton-Johnson, A., Black, M., Fretwell, P. T., and Kaluza-Gilbert, J., 2016. An automated
850 methodology for differentiating rock from snow, clouds and sea in Antarctica from Landsat 8
851 imagery: a new rock outcrop map and area estimation for the entire Antarctic continent, The
852 Cryosphere. 10, 1665-1667. https://doi.org/10.5194/tc-10-1665-2016, 2016.

853 Calanchi, N., De Rosa, R., Mazzuoli, R., Rossi, P., Santacroce, R., Ventura, G., 1993. Silicic
854 magma entering a basaltic magma chamber: eruptive dynamics and magma mixing - an
855 example from Salina (Aeolian islands, Southern Tyrrhenian Sea). Bull. Volcanol. 55, 504-522.
856 https://doi.org/10.1007/BF00304593

857 Colizza, E., Finocchiaro, F., Ivaldi, R., Tolotti, R., 2004. Sedimentazione Fine nella Wood Bay
858 (Mare di Ross Occidentale - Antartide). Atti Assoc. Ital. Oceanol. e Limnol. 137–148.

859 Colizza, E., Finocchiaro, F., Marinoni, L., Menegazzo Vitturi, L., Brambati, A., 2003. Tephra
860 Evidence in Marine Sediments from the Shelf of the Western Ross Sea. Terra Antarct. 8, 121–
861 126.

862 Crosta, X., Koç, N., 2007. Chapter Eight Diatoms: From Micropaleontology to Isotope
863 Geochemistry in: Proxies in Late Cenozoic Paleoceanography. Developments in Marine
864 Geology. pp. 327-369. https://doi.org/10.1016/S1572-5480(07)01013-5

865 Cunningham, W.L., Leventer, A., Andrews, J.T., Jennings, A.E., Licht, K.J., 1999. Late
866 Pleistocene-Holocene marine conditions in the Ross Sea, Antarctica: Evidence from the diatom
867 record. the Holocene. 9, 129-139. https://doi.org/10.1191/095968399675624796

868 De Rosa, R., Donato, P., Gioncada, A., Masetti, M., Santacroce, R., 2003. The Monte Guardia
869 eruption (Lipari, Aeolian Islands): An example of a reversely zoned magma mixing sequence.
870 Bull. Volcanol. 65, 530-543. https://doi.org/10.1007/s00445-003-0281-2

871 Del Carlo, P., Di Roberto, A., D'Orazio, M., Petrelli, M., Angioletti, A., Zanchetta, G., Maggi, V.,

Daga, R., Nazzari, M., Rocchi, S., 2018. Late Glacial-Holocene tephra from southern Patagonia and Tierra del Fuego (Argentina, Chile): A complete textural and geochemical fingerprinting for distal correlations in the Southern Hemisphere. Quat. Sci. Rev. 195, 153-170. https://doi.org/10.1016/j.quascirev.2018.07.028

Del Carlo, P., Di Roberto, A., Di Vincenzo, G., Bertagnini, A., Landi, P., Pompilio, M., Colizza, E., Giordano, G., 2015. Late Pleistocene-Holocene volcanic activity in northern Victoria Land recorded in Ross Sea (Antarctica) marine sediments. Bull. Volcanol. 77, 1-17. https://doi.org/10.1007/s00445-015-0924-0

Di Roberto, A., Colizza, E., Del Carlo, P., Petrelli, M., Finocchiaro, F., Kuhn, G., 2019. First marine cryptotephra in Antarctica found in sediments of the western Ross Sea correlates with englacial tephras and climate records. Sci. Rep. 27, 1969-1982. https://doi.org/10.1038/s41598-019-47188-3

Di Roberto, A., Del Carlo, P., Pompilio, M., 2020. Marine record of Antarctic volcanism from drill cores, in: Smellie, J., Panter, K., Geyer, A. (Eds.), Volcanism in Antarctica: 200 Million Years of Subduction, Rifting and Continental Break-Up. Geological Society, London, Memoirs. *In press*

Domack, E.W., Jacobson, E.A., Shipp, S., Anderson, J.B., 1999. Late Pleistocene-Holocene retreat of the West Antarctic Ice-Sheet system in the Ross Sea: Part 2 - Sedimentologic and stratigraphic signature. Bull. Geol. Soc. Am. 111 (10): 1517-1536. https://doi.org/10.1130/0016-7606(1999)111<1517:LPHROT>2.3.CO;2

Dunbar, N., 2003. Blue Ice Tephra II - Brimstone Peak. https://doi.org/10.7265/N5MG7MDK

Dunbar, N.W., Kurbatov, A. V., 2011. Tephrochronology of the Siple Dome ice core, West Antarctica: Correlations and sources. Quat. Sci. Rev. 30, 1602-1614. https://doi.org/10.1016/j.quascirev.2011.03.015

896 Dunbar, N.W., Zielinski, G.A., Voisins, D.T. 2003. Tephra layers in the Siple Dome and Taylor
897 Dome ice cores, Antarctica: Sources and correlations. J. Geophys. Res. 108, BB.
898 https://doi.org/10.1029/2002jb002056

899 Engwell, S. L., Sparks, R. S. J., Carey, S., 2014. Physical characteristics of tephra layers in the deep
900 sea realm: the Campanian Ignimbrite eruption. Geol. Soc. London, Spec. Publ. 398, 47-64.
901 http://dx.doi.org/10.1144/SP398.7

902 Esser, R.P., Kyle, P.R., 2002. $^{40}Ar/^{39}Ar$ chronology of the McMurdo Volcanic Group at The
903 Pleiades, northern Victoria Land, Antarctica. R. Soc. New Zeal. Bull. 35, 415-418.

904 Fraser, C.I., Terauds, A., Smellie, J., Convey, P., Chown, S.L., 2014. Geothermal activity helps life
905 survive glacial cycles. Proc. Natl. Acad. Sci. 111, 5634-5639.
906 https://doi.org/10.1073/pnas.1321437111

907 Gilbert, J.S., Lane, S.J., 1994. The origin of accretionary lapilli. Bull. Volcanol. 56, 398-411.
908 https://doi.org/10.1007/BF00326465

909 Giordano, G., Lucci, F., Phillips, D., Cozzupoli, D., Runci, V., 2012. Stratigraphy, geochronology
910 and evolution of the Mt. Melbourne volcanic field (North Victoria Land, Antarctica). Bull.
911 Volcanol. 74, 1985-2005. https://doi.org/10.1007/s00445-012-0643-8

912 Golledge, N.R., Menviel, L., Carter, L., Fogwill, C.J., England, M.H., Cortese, G., Levy, R.H.,
913 2014. Antarctic contribution to meltwater pulse 1A from reduced Southern Ocean overturning.
914 Nat. Commun. 5. https://doi.org/10.1038/ncomms6107

915 Griggs, A.J., Davies, S.M., Abbott, P.M., Rasmussen, T.L., Palmer, A.P., 2014. Optimising the use
916 of marine tephrochronology in the North Atlantic: A detailed investigation of the Faroe Marine
917 Ash Zones II, III and IV. Quat. Sci. Rev. 106, 122-139.
918 https://doi.org/10.1016/j.quascirev.2014.04.031

919 Gudmundsson, M., Sigmundsson, F., Bjornsson, H., 1997. Subglacial Volcanic Eruptions. Nature.

389, 954-957.

Hall, B.L., Henderson, G.M., Baroni, C., Kellogg, T.B., 2010. Constant Holocene Southern-Ocean ^{14}C reservoir ages and ice-shelf flow rates. Earth Planet. Sci. Lett. 296(1-2), 115-123. https://doi.org/10.1016/j.epsl.2010.04.054

Harpel, C.J., Kyle, P.R., Dunbar, N.W., 2008. Englacial tephrostratigraphy of Erebus volcano, Antarctica. J. Volcanol. Geotherm. Res. 177, 549-568. https://doi.org/10.1016/j.jvolgeores.2008.06.001

Hillenbrand, C., Moreton, S.G., Caburlotto, A., Pudsey, C.J., Lucchi, R.G., 2008. Volcanic time-markers for Marine Isotopic Stages 6 and 5 in Southern Ocean sediments and Antarctic ice cores : implications for tephra correlations between palaeoclimatic records. Quat. Sci. Rev. 27, 518-540. https://doi.org/10.1016/j.quascirev.2007.11.009

Hillenbrand, C.D., Smith, J.A., Kuhn, G., Esper, O., Gersonde, R., Larter, R.D., Maher, B., Moreton, S.G., Shimmield, T.M., Korte, M., 2010. Age assignment of a diatomaceous ooze deposited in the Western Amundsen Sea embayment after the last glacial maximum. J. Quat. Sci. 25, 280-295. https://doi.org/10.1002/jqs.1308

Iverson, N. A., Kalteyer, D., Dunbar, N. W., Kurbatov, A., Yates, M., 2017. Quaternary Geochronology Advancements and best practices for analysis and correlation of tephra and cryptotephra in ice. Quat. Geochronol. 40, 45-55. https://doi.org/10.1016/j.quageo.2016.09.008

James, M.R., Lane, S.J., Gilbert, J.S., 2003. Density, construction, and drag coefficient of electrostatic volcanic ash aggregates. 108, B9. J. Geophys. Res. Solid Earth. https://doi.org/10.1029/2002jb002011

Jochum, K.P., Pfänder, J., Woodhead, J.D., Willbold, M., Stoll, B., Herwig, K., Amini, M., Abouchami, W., Hofmann, A.W., 2005. MPI-DING glasses: New geological reference materials for in situ Pb isotope analysis. Geochemistry, Geophys. Geosystems. 6(10).

https://doi.org/10.1029/2005GC000995

Kim, J., Park, J.W., Lee, M.J., Lee, J.I., Kyle, P.R., 2019. Evolution of Alkalic Magma Systems: Insight from Coeval Evolution of Sodic and Potassic Fractionation Lineages at the Pleiades Volcanic Complex, Antarctica. J. Petrol. 60, 117-150. https://doi.org/10.1093/petrology/egy108

Kyle, P.R., 1990. The Pleiades, in: Lemasurier, W., Thomson, J.W. (Eds.), Volcanoes of the Antarctic Plate and Southern Oceans. American Geophysical Union.

Kyle, P.R., Rankin, P.C., 1976. Rare earth element geochemistry of Late Cenozoic alkaline lavas of the McMurdo Volcanic Group, Antarctica. Geochim. Cosmochim. Acta. 40, 1497-1507. https://doi.org/10.1016/0016-7037(76)90089-2

Lee, J.Y., Marti, K., Severinghaus, J.P., Kawamura, K., Yoo, H.S., Lee, J.B., Kim, J.S., 2006. A redetermination of the isotopic abundances of atmospheric Ar. Geochim. Cosmochim. Acta. 70, 4507-4512. https://doi.org/10.1016/j.gca.2006.06.1563

LeMasurier, W., Thomson, J.W., Baker, P.E., Kyle, P.R., Rowley, P.J., Smellie, J.L., Verwoerd, W.J., 1990. Volcanoes of the Antarctic Plate and Southern Oceans. American Geophysical Union. https://doi.org/10.1029/AR048

Leventer, A., 2011. The fate of Antarctic “sea ice diatoms” and their use as paleoenvironmental indicators, 121-137. https://doi.org/10.1029/ar073p0121

Leventer, A., Domack, E.W., Ishman, S.E., Brachfeld, S., McClennen, C.E., Manley, P., 1996. Productivity cycles of 200-300 years in the Antarctic Peninsula region: Understanding linkages among the sun, atmosphere, oceans, sea ice, and biota. Bull. Geol. Soc. Am. 108, 1626-1644. https://doi.org/10.1130/0016-7606(1996)108<1626:PCOYIT>2.3.CO;2

Licht, K.J., Jennings, A.E., Andrews, J.T., Williams, K.M., Sea, R., Licht, K.J., Jennings, A.E., Andrews, J.T., Williams, K.M., 1996. Chronology of late Wisconsin ice retreat from the

western Ross Sea, Antarctica. 24(3), 223–226. https://doi.org/10.5329/RECADM.20111002004

Liu, E.J., Cashman, K. V., Rust, A.C., Höskuldsson, A., 2017. Contrasting mechanisms of magma fragmentation during coeval magmatic and hydromagmatic activity: the Hverfjall Fires fissure eruption, Iceland. Bull. Volcanol. 79, 68. https://doi.org/10.1007/s00445-017-1150-8

Lowry, D.P., Golledge, N.R., Bertler, N.A.N., Selwyn Jones, R., McKay, R., 2019. Deglacial grounding-line retreat in the Ross Embayment, Antarctica, controlled by ocean and atmosphere forcing. Sci. Adv. 5(8), eaav8754. https://doi.org/10.1126/sciadv.aav8754

Ludwig, K.R., 2012. Isoplot/Ex version 3.75, A Geochronological Toolkit for Microsoft Excel. Berkeley Geochronol. Cent. Spec. Publ. 5, Berkeley. Geochronology Center, Berkeley, California, 75p.

Lyon, G.L., 1986. Stable isotope stratigraphy of ice cores and the age of the last eruption at mount Melbourne, Antarctica. New Zeal. J. Geol. Geophys. 29, 135-138. https://doi.org/10.1080/00288306.1986.10427528

McCoy, F.W., 1981. Areal Distribution, Redeposition and Mixing of Tephra within Deep-Sea Sediments of the Eastern Mediterranean Sea, in: Self, S., Sparks, R.S.J. (Eds.), Tephra Studies. Springer Netherlands, Dordrecht, pp. 245-254

Mezgec, K., Stenni, B., Crosta, X., Masson-Delmotte, V., Baroni, C., Braida, M., Ciardini, V., Colizza, E., Melis, R., Salvatore, M.C., Severi, M., Scarchilli, C., Traversi, R., Udisti, R., Frezzotti, M., 2017. Holocene sea ice variability driven by wind and polynya efficiency in the Ross Sea. Nat. Commun. 8, 1334. https://doi.org/10.1038/s41467-017-01455-x

Moore, J.G., Peck, D.L., 1962. Accretionary Lapilli in Volcanic Rocks of the Western Continental United States. J. Geol. 70, 182-193. https://doi.org/10.1086/626807

Moreton, S.G., Smellie, J.L., 1998. Identification and correlation of distal tephra layers in deep-sea

992 sediment cores, Scotia Sea, Antarctica. Ann. Glaciol. 27, 285-289.
993 https://doi.org/10.3189/1998AoG27-1-285-289

994 Morgavi, D., Arienzo, I., Montagna, C., Perugini, D., Dingwell, D.B., 2019. Magma Mixing:
995 History and Dynamics of an Eruption Trigger, in: Gottsmann, J., Neuberg, J., Scheu, B. (Eds.),
996 Volcanic Unrest : From Science to Society. Springer International Publishing, Cham. pp. 123-
997 137. https://doi.org/10.1007/11157_2017_30

998 Murphy, M.D., Sparks, R.S.J., Barclay, J., Carroll, M.R., Brewer, T.S., 2000. Remobilization of
999 andesite magma by intrusion of mafic magma at the Soufriere Hills volcano, Montserrat, West
1000 Indies. J. Petrol. 41, 21-42. https://doi.org/10.1093/petrology/41.1.21

1001 Murphy, M.D., Sparks, R.S.J., Barclay, J., Carroll, M.R., Lejeune, A.M., Brewer, T.S., Macdonald,
1002 R., Black, S., Young, S., 1998. The role of magma mixing in triggering the current eruption at
1003 the Soufriere Hills Volcano, Montserrat, West Indies. Geophys. Res. Lett. 25, 3433-3436.
1004 https://doi.org/10.1029/98GL00713

1005 Murtagh, R.M., White, J.D.L., 2013. Pyroclast characteristics of a subaqueous to emergent
1006 Surtseyan eruption, black point volcano, california. J. Volcanol. Geotherm. Res. 267, 75-91.
1007 https://doi.org/10.1016/j.jvolgeores.2013.08.015

1008 Narcisi, B., Petit, J.R., Delmonte, B., Scarchilli, C., Stenni, B., 2012. A 16,000-yr tephra framework
1009 for the Antarctic ice sheet: A contribution from the new Talos Dome core. Quat. Sci. Rev. 49,
1010 52-63. https://doi.org/10.1016/j.quascirev.2012.06.011

1011 Narcisi, B., Petit, J.R., Langone, A., 2017. Last glacial tephra layers in the Talos Dome ice core
1012 (peripheral East Antarctic Plateau), with implications for chronostratigraphic correlations and
1013 regional volcanic history. Quat. Sci. Rev. 165, 111-126.
1014 https://doi.org/10.1016/j.quascirev.2017.04.025

1015 Nathan, S., Schulte, F.J., 1968. Geology and petrology of the Campbell—Aviator Divide, Northern

1016 Victoria Land, Antarctica. New Zeal. J. Geol. Geophys. 11, 940-975.
1017 https://doi.org/10.1080/00288306.1968.10420762

1018 Niespolo, E.M., Rutte, D., Deino, A.L., Renne, P.R., 2017. Intercalibration and age of the Alder
1019 Creek sanidine $^{40}Ar/^{39}Ar$ standard. Quat. Geochronol. 39, 205-213.
1020 https://doi.org/10.1016/j.quageo.2016.09.004

1021 Oppedal, L.T., van der Bilt, W.G.M., Balascio, N.L., Bakke, J., 2018. Patagonian ash on sub-
1022 Antarctic South Georgia: expanding the tephrostratigraphy of southern South America into the
1023 Atlantic sector of the Southern Ocean. J. Quat. Sci. 33, 482-486.
1024 https://doi.org/10.1002/jqs.3035

1025 Palais, J.M., Kyle, P.R., Mosley-Thompson, E., Thomas, E., 1987. Correlation of a 3,200 year old
1026 tephra in ice cores from Vostok and South Pole Stations, Antarctica. Geophys. Res. Lett. 14,
1027 804-807. https://doi.org/10.1029/GL014i008p00804

1028 Perkins, M.E., Nash, W.P., Brown, F.H., Fleck, R.J., 1995. Fallout tuffs of Trapper Creek, Idaho - a
1029 record of Miocene explosive volcanism in the Snake River Plain volcanic province. Geol. Soc.
1030 Am. Bull. 107, 1484-1506. https://doi.org/10.1130/0016-
1031 7606(1995)107<1484:FTOTCI>2.3.CO;2

1032 Pike, J., Crosta, X., Maddison, E.J., Stickley, C.E., Denis, D., Barbara, L., Renssen, H., 2009.
1033 Observations on the relationship between the Antarctic coastal diatoms Thalassiosira antarctica
1034 Comber and Porosira glacialis (Grunow) Jørgensen and sea ice concentrations during the late
1035 Quaternary. Mar. Micropaleontol. 73, 14-25. https://doi.org/10.1016/j.marmicro.2009.06.005

1036 Pudsey, C.J., Murray, J.W., Appleby, P., Evans, J., 2006. Ice shelf history from petrographic and
1037 foraminiferal evidence, Northeast Antarctic Peninsula. Quat. Sci. Rev. 25, 2357-2379.
1038 https://doi.org/10.1016/j.quascirev.2006.01.029

1039 Rathburn, A.E., Pichon, J.J., Ayress, M.A., De Deckker, P., 1997. Microfossil and stable-isotope

1040 evidence for changes in Late Holocene palaeoproductivity and palaeoceanographic conditions
1041 in the Prydz Bay region of Antarctica. Palaeogeogr. Palaeoclimatol. Palaeoecol. 131, 485-510.
1042 https://doi.org/10.1016/S0031-0182(97)00017-5

1043 Riddolls, B.W., Hancox, G.T., 1968. The geology of the upper Mariner Glacier region, North
1044 Victoria Land, Antarctica. New Zeal. J. Geol. Geophys. 11, 881-899.
1045 https://doi.org/10.1080/00288306.1968.10420758

1046 Russell, J.K., Edwards, B.R., Porritt, L.A., 2013. Pyroclastic passage zones in glaciovolcanic
1047 sequences. Nat. Commun. 4, 1788. https://doi.org/10.1038/ncomms2829

1048 Sarna-Wojcicki, A.M., Morrison, S.D., Meyer, C.E., Hillhouse, J.W., 1987. Correlation of upper
1049 Cenozoic tephra layers between sediments of the western United States and eastern Pacific
1050 Ocean and comparison with biostratigraphic and magnetostratigraphic age data. Geol. Soc.
1051 Am. Bull. 98(2), 207-223. https://doi.org/10.1130/0016-
1052 7606(1987)98<207:COUCTL>2.0.CO;2

1053 Schumacher, R., Schmincke, H.U., 1995. Models for the origin of accretionary lapilli. Bull.
1054 Volcanol. 56, 626-639. https://doi.org/10.1007/BF00301467

1055 Schumacher, R., Schmincke, H.U., 1991. Internal structure and occurrence of accretionary lapilli - a
1056 case study at Laacher See Volcano. Bull. Volcanol. 53, 612-634.
1057 https://doi.org/10.1007/BF00493689

1058 Self, S., 1983. Large-scale phreatomagmatic silicic volcanism: A case study from New Zealand. J.
1059 Volcanol. Geotherm. Res. 17, 433-469. https://doi.org/10.1016/0377-0273(83)90079-3

1060 Self, S., Sparks, R.S.J., 1978. Characteristics of widespread pyroclastic deposits formed by the
1061 interaction of silicic magma and water. Bull. Volcanol. 41, 196-212.
1062 https://doi.org/10.1007/BF02597223

1063 Sheridan, M.F., Wohletz, K.H., 1983. Hydrovolcanism: Basic considerations and review. J.

1064 Volcanol. Geotherm. Res. 17, 1-29. https://doi.org/10.1016/0377-0273(83)90060-4

1065 Sigl, M., Fudge, T.J., Winstrup, M., Cole-Dai, J., Ferris, D., McConnell, J.R., Taylor, K.C., Welten,
1066 K.C., Woodruff, T.E., Adolphi, F., Bisiaux, M., Brook, E.J., Buizert, C., Caffee, M.W.,
1067 Dunbar, N.W., Edwards, R., Geng, L., Iverson, N., Koffman, B., Layman, L., Maselli, O.J.,
1068 McGwire, K., Muscheler, R., Nishiizumi, K., Pasteris, D.R., Rhodes, R.H., Sowers, T.A.,
1069 2016. The WAIS Divide deep ice core WD2014 chronology - Part 2: Annual-layer counting
1070 (0-31 ka BP). Clim. Past. 12, 769-786. https://doi.org/10.5194/cp-12-769-2016

1071 Smellie, J.L., Skilling, I.P., 1994. Products of subglacial volcanic eruptions under different ice
1072 thicknesses: two examples from Antarctica. Sediment. Geol. https://doi.org/10.1016/0037-
1073 0738(94)90125-2

1074 Steiger, R.H., Jäger, E., 1977. Subcommission on geochronology: Convention on the use of decay
1075 constants in geo- and cosmochronology. Earth Planet. Sci. Lett. 91, 115-129.
1076 https://doi.org/10.1016/0012-821X(77)90060-7

1077 Stuiver, M., Reimer, P.J., Reimer, R.W., 2019. CALIB 7.1 [WWW program] [WWW Document].
1078 http://calib.org.

1079 Tesi, T., Belt, S.T., Gariboldi, K., Muschitiello, F., Smik, L., Finocchiaro, F., Giglio, F., Colizza,
1080 E., Gazzurra, G., Giordano, P., Morigi, C., Capotondi, L., Nogarotto, A., Köseoğlu, D., Di
1081 Roberto, A., Gallerani, A., Langone, L., 2020. Resolving sea ice dynamics in the north-western
1082 Ross Sea during the last 2.6 ka: From seasonal to millennial timescales. Quat. Sci. Rev. 237,
1083 106299. https://doi.org/10.1016/J.QUASCIREV.2020.106299

1084 Textor, C., Graf, H.F., Herzog, M., Oberhuber, J.M., Rose, W.I., Ernst, G.G.J., 2006. Volcanic
1085 particle aggregation in explosive eruption columns. Part I: Parameterization of the
1086 microphysics of hydrometeors and ash. J. Volcanol. Geotherm. Res. 150, 359-377.
1087 https://doi.org/10.1016/j.jvolgeores.2005.09.007

1088 Tomlinson, E.L., Thordarson, T., Müller, W., Thirlwall, M., Menzies, M.A., 2010. Microanalysis of
1089 tephra by LA-ICP-MS — Strategies, advantages and limitations assessed using the Thorsmörk
1090 ignimbrite (Southern Iceland). Chem. Geol. 279, 73-89.
1091 https://doi.org/10.1016/j.chemgeo.2010.09.013

1092 Tuffen, H., 2010. How will melting of ice affect volcanic hazards in the twenty-first century?
1093 Philos. Trans. R. Soc. A. 368, 2535-2558. https://doi.org/10.1098/rsta.2010.0063

1094 Van Der Bilt, W.G.M., Lane, C.S., 2019. Lake sediments with Azorean tephra reveal ice-free
1095 conditions on coastal northwest Spitsbergen during the Last Glacial Maximum. Sci. Adv.
1096 5(10), eaaw5980. https://doi.org/10.1126/sciadv.aaw5980

1097 Van Eaton, A.R., Wilson, C.J.N., 2013. The nature, origins and distribution of ash aggregates in a
1098 large-scale wet eruption deposit: Oruanui, New Zealand. J. Volcanol. Geotherm. Res. 250,
1099 129-154. https://doi.org/10.1016/j.jvolgeores.2012.10.016

1100 Veitch, G., Woods, A.W., 2001. Particle aggregation in volcanic eruption columns. J. Geophys.
1101 Res. Solid Earth. 106, 26425-26441. https://doi.org/10.1029/2000jb900343

1102 Wacker, L., Fahrni, S. M., Hajdas, I., Molnar, M., Synal, H. A., Szidat, S., Zhang, Y. L., 2013. A
1103 versatile gas interface for routine radiocarbon analysis with a gas ion source. Nucl. Instrum.
1104 Methods Phys. Res. 294, 315-319. https://doi.org/10.1016/j.nimb.2012.02.009.

1105 Walker, G.P.L., 1981. Characteristics of two phreatoplinian ashes, and their water-flushed origin. J.
1106 Volcanol. Geotherm. Res. 9, 395-407. https://doi.org/10.1016/0377-0273(81)90046-9

1107 White, J.D.L., 1996. Pre-emergent construction of a lacustrine basaltic volcano, Pahvant Butte, Utah
1108 (USA). Bull. Volcanol. 58, 249-262. https://doi.org/10.1007/s004450050138

1109

1110

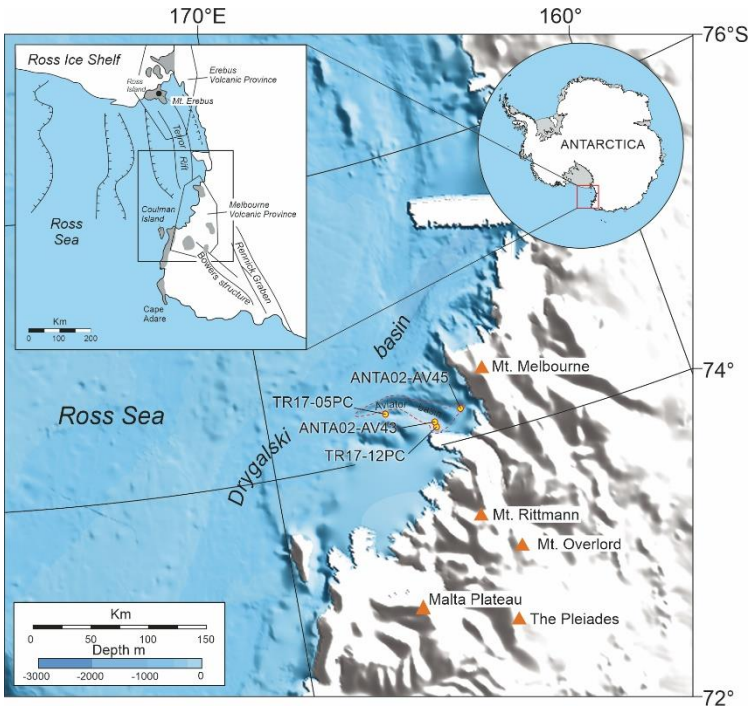
170°E
160°
76°S
74°
72°
Ross Ice Shelf
Erebus Volcanic Province
Ross Island
Mt. Erebus
Taylor Flm
Coulman Island
Melbourne Volcanic Province
Ross Sea
Terror Graben
Discovery structure
Cape Adare
Km
0 100 200
ANTARCTICA
basin
Mt. Melbourne
ANTA02-AV45
TR17-05PC
Nansen
ANTA02-AV43
TR17-12PC
Ross Sea
Drygalski
Mt. Rittmann
Mt. Overlord
Malta Plateau
The Pleiades
Km
0 50 100 150
Depth m
-3000 -2000 -1000 0

1111

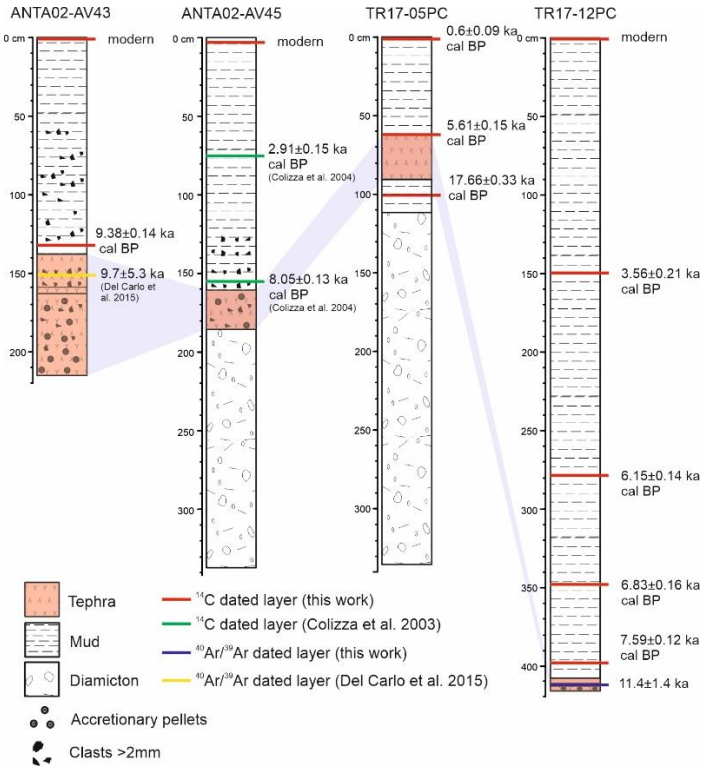
ANTA02-AV43
ANTA02-AV45
TR17-05PC
TR17-12PC
modern
9.38±0.14 ka cal BP
9.7±5.3 ka (Del Carlo et al. 2015)
2.91±0.15 ka cal BP (Colizza et al. 2004)
8.05±0.13 ka cal BP (Colizza et al. 2004)
0.6±0.09 ka cal BP
5.61±0.15 ka cal BP
17.66±0.33 ka cal BP
3.56±0.21 ka cal BP
6.15±0.14 ka cal BP
6.83±0.16 ka cal BP
7.59±0.12 ka cal BP
11.4±1.4 ka
Tephra
Mud
Diamicton
14C dated layer (this work)
14C dated layer (Colizza et al. 2003)
40Ar/39Ar dated layer (this work)
40Ar/39Ar dated layer (Del Carlo et al. 2015)
Accretionary pellets
Clasts >2mm

1112

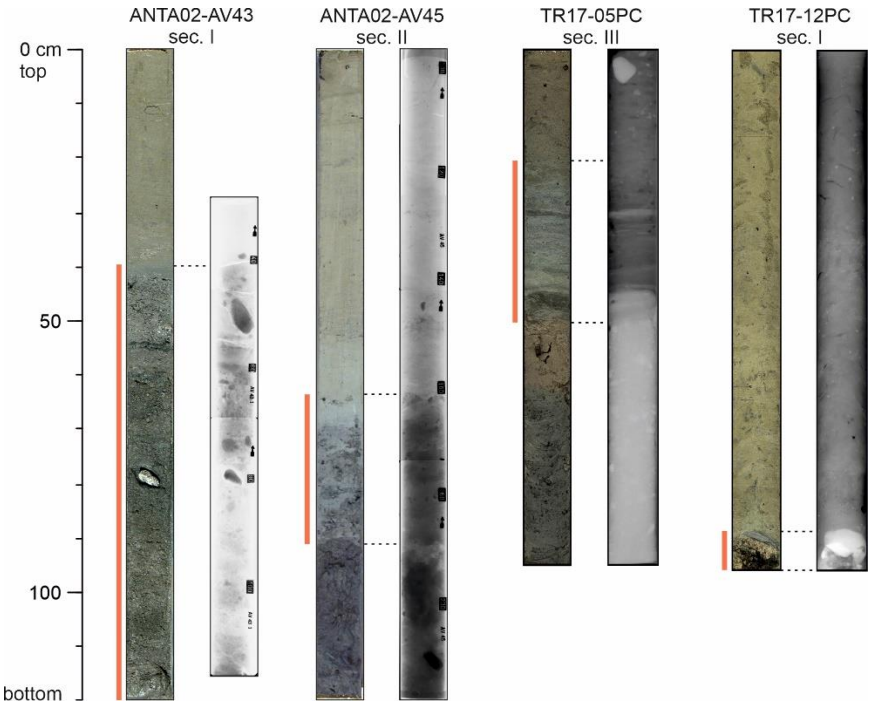
ANTA02-AV43
sec. I
ANTA02-AV45
sec. II
TR17-05PC
sec. III
TR17-12PC
sec. I
0 cm
top
50
100
bottom

1113

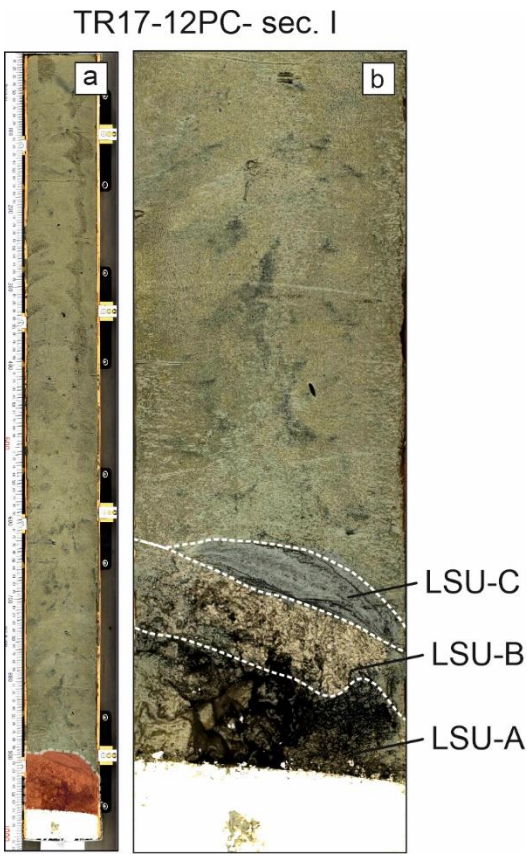
TR17-12PC- sec. I
a
b
LSU-C
LSU-B
LSU-A

1114

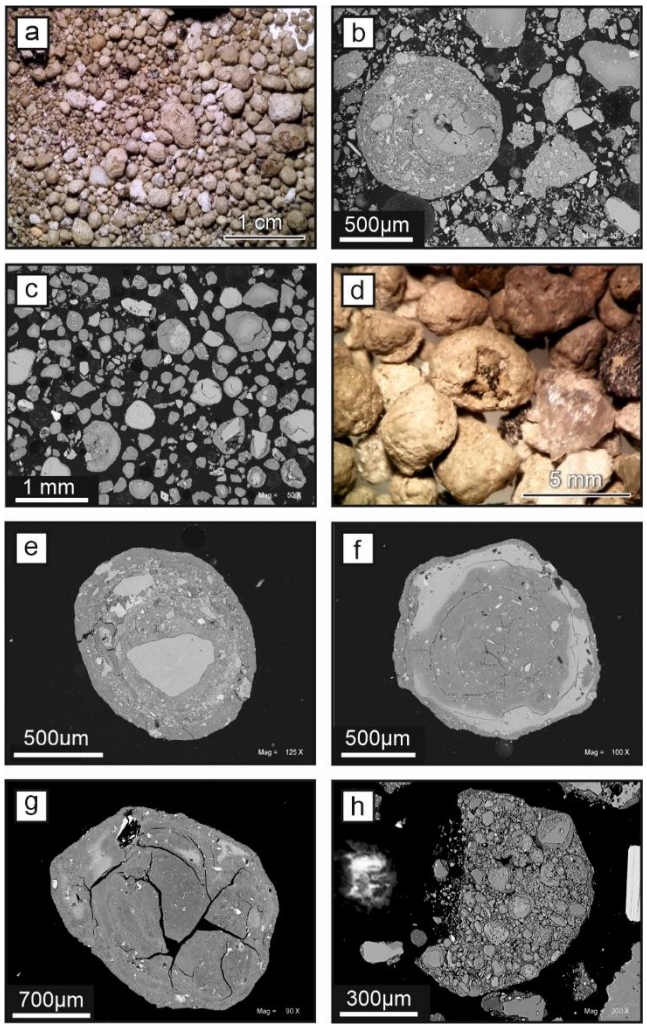
a
1 cm
b
500µm
c
1 mm
d
5 mm
e
500um
f
500µm
g
700µm
h
300µm

1115

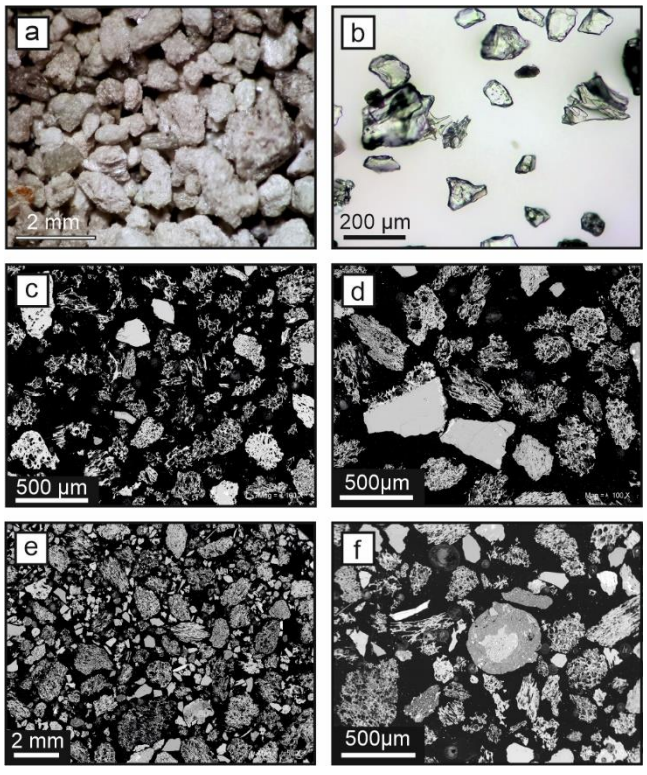
a
2 mm
b
200 µm
c
500 µm
d
500µm
e
2 mm
f
500µm

1116

1117

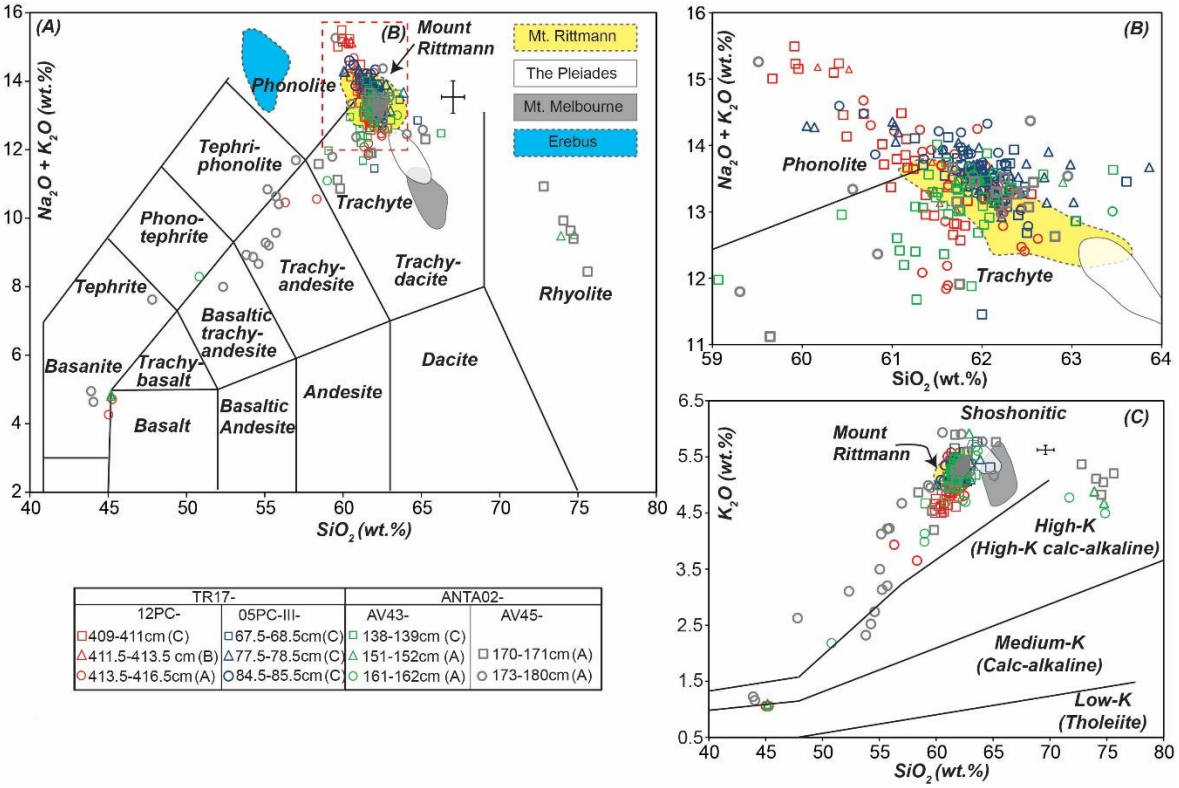

TR17-		ANTA02-	
12PC-	05PC-III-	AV43-	AV45-
□409-411cm (C)	□67.5-68.5cm(C)	□138-139cm (C)	
△411.5-413.5 cm (B)	△77.5-78.5cm (C)	△151-152cm (A)	□170-171cm (A)
○413.5-416.5cm (A)	○84.5-85.5cm (C)	○161-162cm (A)	○173-180cm (A)

1118

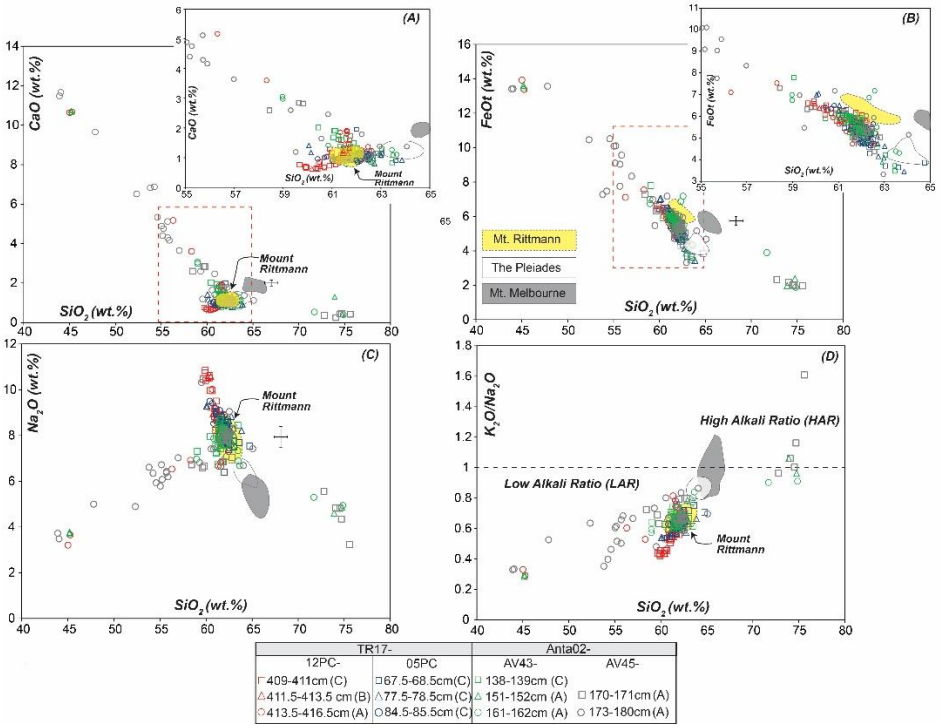
(A)
CaO (wt.%)
SiO2 (wt.%)
Mount Rittmann
(B)
FeOt (wt.%)
Mt. Rittmann
The Pleiades
Mt. Melbourne
(C)
Na2O (wt.%)
(D)
K2O/Na2O
High Alkali Ratio (HAR)
Low Alkali Ratio (LAR)
TR17-
12PC-
409-411cm (C)
411.5-413.5 cm (B)
413.5-416.5cm (A)
05PC
67.5-68.5cm(C)
77.5-78.5cm(C)
84.5-85.5cm(C)
Anta02-
AV43-
138-139cm (C)
151-152cm (A)
161-162cm (A)
AV45-
170-171cm (A)
173-180cm (A)

1119

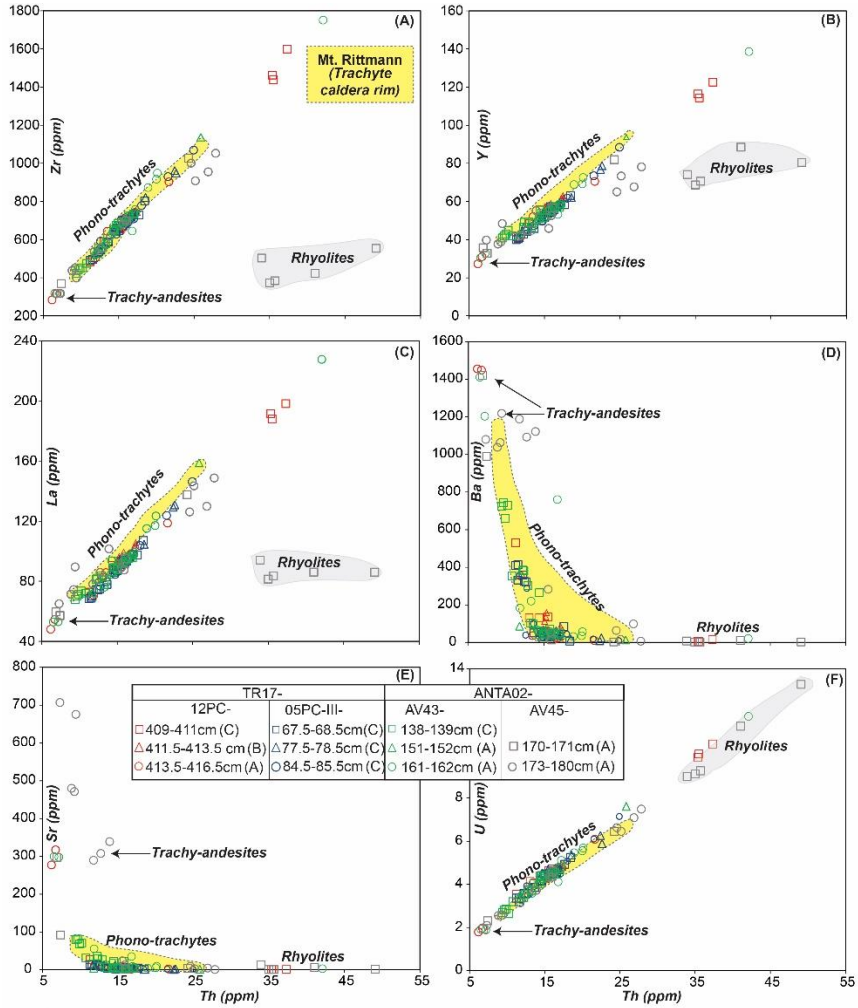
(A)
Mt. Rittmann
(Trachyte caldera rim)
Zr (ppm)
Phono-trachytes
Rhyolites
Trachy-andesites
(B)
Y (ppm)
(C)
La (ppm)
(D)
Ba (ppm)
(E)
Sr (ppm)
Th (ppm)
(F)
U (ppm)
TR17-
12PC-
409-411cm (C)
411.5-413.5 cm (B)
413.5-416.5cm (A)
05PC-III-
67.5-68.5cm(C)
77.5-78.5cm(C)
84.5-85.5cm(C)
ANTA02-
AV43-
138-139cm (C)
151-152cm (A)
161-162cm (A)
AV45-
170-171cm (A)
173-180cm (A)

1120

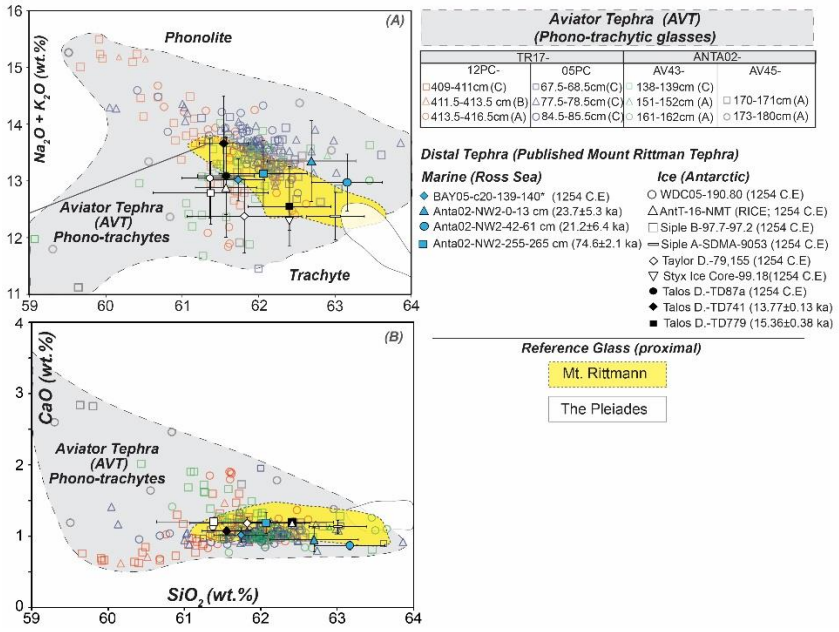
(A)
Phonolite
Trachyte
Aviator Tephra (AVT) Phono-trachytes
$Na_2O + K_2O$ (wt.%)
(B)
CaO (wt.%)
SiO_2 (wt.%)
Aviator Tephra (AVT) (Phono-trachytic glasses)
TR17-
ANTA02-
12PC-
05PC
AV43-
AV45-
409-411cm (C)
411.5-413.5 cm (B)
413.5-416.5cm (A)
67.5-68.5cm(C)
77.5-78.5cm (C)
84.5-85.5cm (C)
138-139cm (C)
151-152cm (A)
161-162cm (A)
170-171cm (A)
173-180cm (A)
Distal Tephra (Published Mount Rittman Tephra)
Marine (Ross Sea)
BAY05-c20-139-140* (1254 C.E)
Anta02-NW2-0-13 cm (23.7±5.3 ka)
Anta02-NW2-42-61 cm (21.2±6.4 ka)
Anta02-NW2-255-265 cm (74.6±2.1 ka)
Ice (Antarctic)
WDC05-190.80 (1254 C.E)
AntT-16-NMT (RICE; 1254 C.E)
Siple B-97.7-97.2 (1254 C.E)
Siple A-SDMA-9053 (1254 C.E)
Taylor D.-79,155 (1254 C.E)
Styx Ice Core-99.18(1254 C.E)
Talos D.-TD87a (1254 C.E)
Talos D.-TD741 (13.77±0.13 ka)
Talos D.-TD779 (15.36±0.38 ka)
Reference Glass (proximal)
Mt. Rittmann
The Pleiades

1121

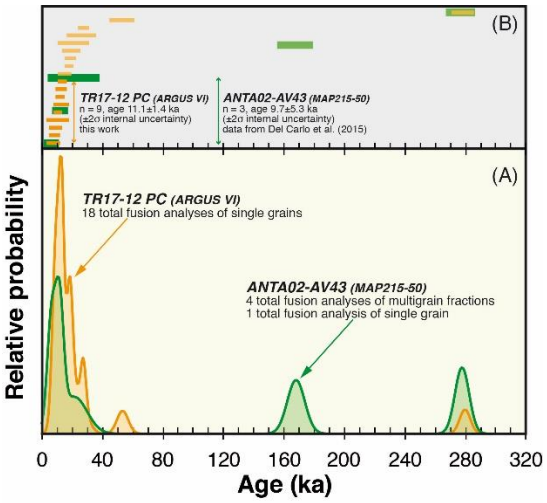
(B)
TR17-12 PC (ARGUS VI)
n = 9, age 11.1±1.4 ka
(±2σ internal uncertainty)
this work
ANTA02-AV43 (MAP215-50)
n = 3, age 9.7±5.3 ka
(±2σ internal uncertainty)
data from Del Carlo et al. (2015)
(A)
TR17-12 PC (ARGUS VI)
18 total fusion analyses of single grains
ANTA02-AV43 (MAP215-50)
4 total fusion analyses of multigrain fractions
1 total fusion analysis of single grain
Relative probability
0
40
80
120
160
200
240
280
320
Age (ka)

1122

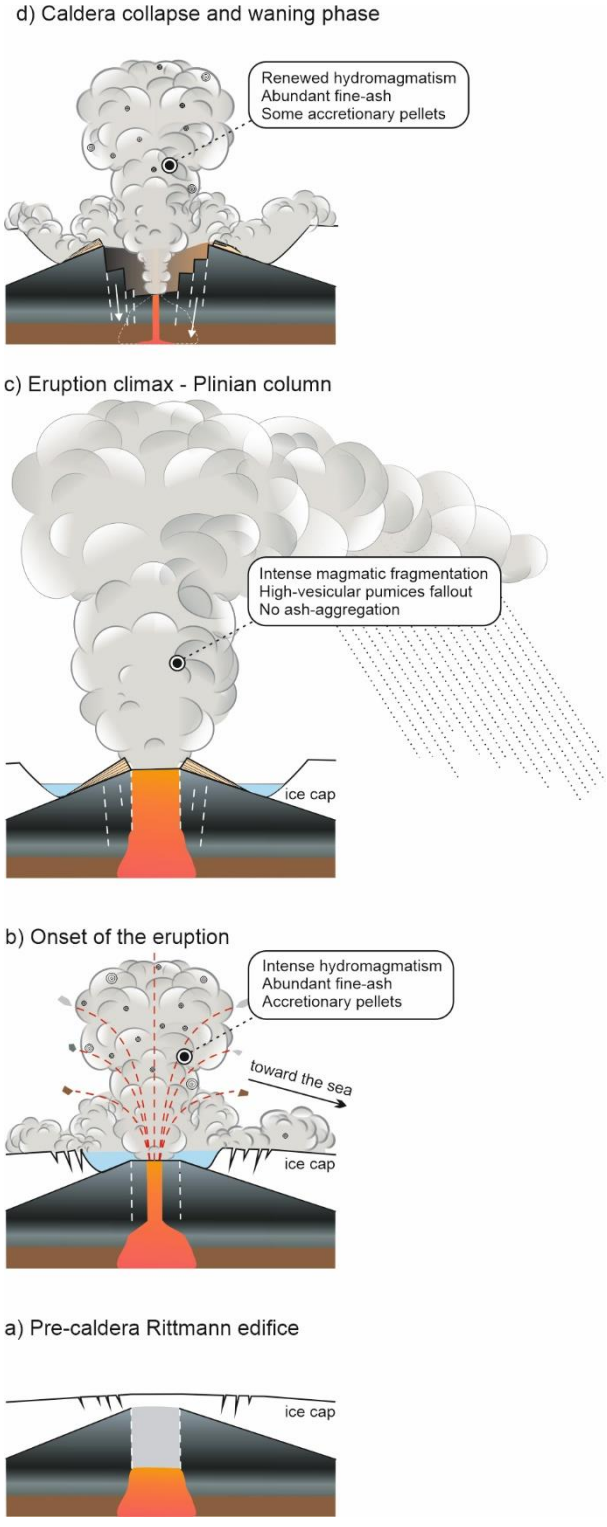

1123

1124

1125

1126

Table 1 - Position of the studied cores and depth interval for Lithostratigraphic Units (LSU)

Core	ANTA02-AV43			ANTA02-AV45	TR17-05PC	TR17-12PC		
Latitude	-74.141			-74.207	-74.299	-74.147		
Longitude	166.083			165.592	166.799	166.089		
Water depth (m):	916			648	777	912		
Core Length (m)	218			339	344	450		
Tephra depth interval	137-148	148-151	151-215	161-187	62.5-90.5	409-411	411-413.5	413.5-416.5
LSU	C	B	A	A	C	C	B	A
Thickness (cm)	11	3	64	26	30	2	~3	3

Table 2. Radiocarbon dates and sedimentation rate modeled for cores ANTA02-AV43, ANTA02-AV45, TR17-5PC, TR17-12PC and box cores BAY05-bc40 and TR17-05bc.

Core and box-core ID	Sample depth (cm)	Sediment facies[a]	Carbon source[b]	Laboratory name	Conventional ^{14}C age (yrs BP)	$\delta^{13}C$	LCO[c]	LCO corr. Age (yr BP)	Calibrated age (yr BP)[d]	1 sigma range		1 σ error	median probability	sedimentation rate cm/yr
ANTA02-AV43	0-1	DO	AIO	AWI-4826.1.1	1878 ± 37	-22.7	1090	788	modern	-	-	-	-	-
ANTA02-AV43	130-131	DO	AIO	Poz-111983	10620 ± 60	-	1090	9530	9380	9238	9532	147	9390	0.014
ANTA02-AV45	3-4	DO	AIO	AWI-4827.1.1	2256 ± 38	-20.5	1090	1166	modern	-	-	-	-	-
ANTA02-AV45	73-74	DO	AIO	from Colizza et al., 2004	5010 ± 40	-28.0	1090	3920	2910	2763	3063	150	2933	0.024
ANTA02-AV45	156-157	DO	AIO	from Colizza et al., 2004	9460 ± 50	-26.7	1090	8370	8050	7914	8178	132	8046	0.016
BAY05-bc40	0-1	DO	AIO	from Mezgec et al., 2017	2230± 30	-24.4	-	-	-	-	-	-	-	-
TR17-05PC	0-1	DO	AIO	AWI-4823.1.2	3620 ± 20	-26.0	1805	1815	600	503	690	94	607	-
TR17-05PC	62-63	DO	AIO	Poz-111982	7850 ± 50	-	1805	6045	5610	5463	5756	147	5623	0.012
TR17-05PC	98--99	DO	AIO	AWI-4824.1.2	17514 ± 240	-18.7	1805	15709	17660	17327	18000	337	17657	0.001*
TR17-05bc	0-1	DO	AIO	Poz-111980	2945 ± 30	-	-	-	-	-	-	-	-	-
TR17-12PC	0-1	DO	AIO	AWI-4825.1.1	2093 ± 37	-21.3	1090	1003	modern	-	-	-	-	-
TR17-12PC	149-150	DO	AIO	Poz-111975	5570 ± 40	-	1090	4480	3560	3347	3766	210	3613	0.042
TR17-12PC	257-258	DO	AIO	Poz-111976	7640 ± 40	-	1090	6550	6150	6009	6287	139	6163	0.042
TR17-12PC	347-348	DO	AIO	Poz-111977	8240 ± 50	-	1090	7150	6830	6666	6985	160	6836	0.135
TR17-12PC	397-398	DO	AIO	Poz-111979	9000 ± 50	-	1090	7910	7590	7472	7712	120	7602	0.064

a. DO = diatomaceous ooze; b. AIO = acid-insoluble organic matter; c. LCO = local contamination offset (see text); d. calibrated ages using CALIB REV 7.1.0 (Stuiver *et al*., 2019). All the ages are in years BP (1950 AD) and rounded to the nearest ten years * sedimentation rate calculated without considering the tephra

Table 3. ^{40}Ar-^{39}Ar data on alkali feldspar of AVT tephra in core TR17-12PC. Relative abundances

	^{36}Ar	±1σ	^{37}Ar	±1σ	^{38}Ar	±1σ	^{39}Ar	±1σ	^{40}Ar	±1σ	$^{40}Ar^*/^{39}Ar(k)$	±2σ	Age	±2σ	$^{40}Ar^*$	$^{39}Ar_{(K)}$	K/Ca	±2σ
	[fA]		[fA]		[fA]		[fA]		[fA]				(Ma)		(%)	(%)		
J = 0.00019866 ± 0.00000024																		
Total fusion analysis of single grains																		
143A	6.97E-01	1.36E-03	4.28E+00	4.81E-02	1.33E+00	3.34E-02	9.50E+01	1.61E-02	2.14E+02	4.35E-02	0.0535	0.0098	19.18	3.50	2.4	9.0	11.8	1.2
143B	6.90E-01	1.70E-03	3.80E+00	4.78E-02	2.01E+00	3.31E-02	1.49E+02	2.66E-02	2.13E+02	3.30E-02	0.0371	0.0075	13.30	2.69	2.6	14.2	20.8	2.1
143C	2.59E-01	7.96E-04	9.54E-01	3.04E-02	7.83E-01	3.61E-02	5.54E+01	1.50E-02	8.07E+01	2.58E-02	0.0501	0.0092	17.96	3.30	3.4	5.3	30.8	3.6
143H	3.14E-01	1.00E-03	1.32E+00	5.46E-02	7.55E-01	2.40E-02	5.51E+01	1.51E-02	9.64E+01	2.83E-02	0.0421	0.0115	15.10	4.13	2.4	5.2	22.1	2.9
143I	3.81E-01	1.01E-03	1.39E+00	3.63E-02	1.09E+00	2.86E-02	8.02E+01	1.79E-02	1.17E+02	7.69E-02	0.0293	0.0084	10.49	3.00	2.0	7.6	30.6	3.5
143K	1.81E-01	8.56E-04	1.49E+00	5.51E-02	7.95E-01	2.79E-02	5.89E+01	1.52E-02	5.66E+01	3.43E-02	0.0343	0.0091	12.30	3.26	3.6	5.6	20.9	2.6
143P	1.69E-01	7.70E-04	8.57E-01	3.79E-02	5.20E-01	2.00E-02	4.43E+01	1.26E-02	5.17E+01	3.25E-02	0.0213	0.0108	7.65	3.88	1.8	4.2	27.4	3.7
143Q	5.06E-01	8.20E-04	2.36E+00	4.31E-02	6.92E-01	2.34E-02	4.79E+01	1.50E-02	1.53E+02	3.60E-02	0.0249	0.0122	8.93	4.38	0.8	4.6	10.7	1.1
143S	4.94E-01	1.19E-03	1.37E+00	4.24E-02	1.11E+00	2.15E-02	7.97E+01	1.68E-02	1.50E+02	3.88E-02	0.0245	0.0098	8.76	3.53	1.3	7.6	30.9	3.6
143U	2.87E-01	1.14E-03	5.20E-01	4.15E-02	6.14E-01	2.59E-02	4.70E+01	1.36E-02	8.78E+01	3.26E-02	0.0342	0.0150	12.26	5.39	1.8	4.5	47.9	9.0
143W	4.78E-01	1.07E-03	3.15E+00	4.88E-02	1.00E+00	2.24E-02	7.03E+01	1.79E-02	1.49E+02	4.45E-02	0.0761	0.0101	27.28	3.64	3.6	6.7	11.8	1.2
143X	2.57E-01	7.51E-04	5.01E-01	4.01E-02	7.90E-01	2.25E-02	5.69E+01	1.64E-02	7.94E+01	3.44E-02	0.0355	0.0086	12.74	3.07	2.5	5.4	60.3	11.4
197B	3.63E-01	1.27E-03	1.01E+00	8.08E-02	7.48E-01	2.64E-02	4.88E+01	1.75E-02	1.11E+02	3.42E-02	0.0540	0.0163	19.36	5.85	2.4	4.6	25.6	4.8
197C	7.54E-01	2.13E-03	2.03E+00	8.45E-02	7.65E-01	2.15E-02	4.70E+01	1.76E-02	2.28E+02	3.86E-02	0.0597	0.0287	21.4	10.3	1.2	4.5	12.3	1.6
197E	1.14E-01	8.86E-04	6.14E-01	4.05E-02	4.03E-01	3.20E-02	2.72E+01	1.47E-02	3.52E+01	3.94E-02	0.0293	0.0199	10.49	7.13	2.3	2.6	23.5	3.9
197F	1.48E-01	9.86E-04	1.24E+00	6.54E-02	3.54E-01	3.43E-02	2.31E+01	1.38E-02	4.61E+01	3.81E-02	0.0739	0.0260	26.50	9.33	3.7	2.2	9.9	1.4
197H	1.09E-01	9.77E-04	6.27E-01	8.02E-02	5.69E-01	2.70E-02	2.96E+01	1.51E-02	5.58E+01	3.09E-02	0.7804	0.0200	279.69	7.17	41.5	2.8	25.0	6.9
197I	2.37E-01	1.20E-03	1.74E+00	7.99E-02	4.99E-01	2.96E-02	3.48E+01	1.60E-02	7.61E+01	3.45E-02	0.1485	0.0210	53.23	7.54	6.8	3.3	10.6	1.4

laser power W	^{36}Ar	±1σ	^{37}Ar	±1σ	^{38}Ar	±1σ	39Ar	±1σ	^{40}Ar	±1σ	$^{40}Ar^*/^{39}Ar(k)$	±2σ	Age	±2σ	$^{40}Ar^*$	$^{39}Ar(K)$	K/Ca	±2σ
	[fA]		[fA]		[fA]		[fA]		[fA]				(Ma)		(%)	(%)		
step-heating analyses																		
3 grains																		

165J	1.5	1.78E+00	9.52E-03	8.21E-01	8.38E-02	5.10E-01	3.12E-02	1.23E+01	1.95E-02	5.34E+02	5.67E-02	0.2726	0.4691	98	168	0.6	6.1	8.0	1.8
165K	2.5	4.51E-02	8.92E-04	2.30E+00	6.71E-02	7.71E-01	3.27E-02	5.86E+01	2.26E-02	1.58E+01	3.36E-02	0.0331	0.0093	11.85	3.34	12.3	29.1	13.5	1.6
165M	3.5	6.76E-03	8.18E-04	1.95E+00	5.36E-02	6.56E-01	2.64E-02	5.22E+01	2.11E-02	4.24E+00	3.25E-02	0.0357	0.0096	12.80	3.43	44.0	25.9	14.2	1.6
165N	5	5.84E-03	7.61E-04	2.31E+00	5.42E-02	7.81E-01	2.50E-02	6.06E+01	1.74E-02	5.38E+00	3.01E-02	0.0532	0.0077	19.05	2.77	59.9	30.1	13.9	1.5
165U	fuse	3.91E-03	8.22E-04	3.61E-01	5.11E-02	2.48E-01	3.52E-02	1.76E+01	9.77E-03	1.49E+00	3.01E-02	0.0100	0.0281	3.6	10.1	11.9	8.8	25.9	7.8
total gas												**0.0525**	**0.0290**	**18.8**	**10.5**			**13.8**	**1.5**
1 grain																			
165V	2.0	7.76E-01	1.45E-03	2.36E-01	4.28E-02	2.66E-01	2.24E-02	4.31E+00	1.00E-02	2.31E+02	3.83E-02	-0.1396	0.2287	-50	82	-0.3	3.1	9.7	3.6
165X	3.0	1.02E-02	5.52E-04	8.97E-01	3.75E-02	5.83E-01	2.57E-02	4.16E+01	1.26E-02	5.82E+00	2.48E-02	0.0585	0.0082	21.0	2.9	41.8	29.9	24.6	3.2
165Y	fuse	1.39E-01	9.18E-04	1.74E+00	5.24E-02	1.20E+00	2.93E-02	9.32E+01	2.26E-02	4.59E+01	3.28E-02	0.0380	0.0062	13.6	2.2	7.7	67.0	28.3	3.3
total gas												**0.0387**	**0.0086**	**13.9**	**3.1**			**25.6**	**2.9**
1 grain																			
166A	2.0	4.70E-01	1.24E-03	1.54E-01	4.24E-02	1.43E-01	2.81E-02	4.40E+00	1.78E-02	1.40E+02	3.72E-02	-0.0048	0.1810	-2	65	0.0	7.6	15.1	8.4
166B	3.0	3.65E-03	8.86E-04	3.74E-01	5.32E-02	2.18E-01	3.85E-02	1.66E+01	1.54E-02	2.11E+00	3.13E-02	0.0535	0.0322	19	12	42.1	28.7	23.5	7.1
166D	fuse	1.04E-02	7.45E-04	8.43E-01	5.14E-02	5.05E-01	2.97E-02	3.67E+01	1.17E-02	5.49E+00	3.13E-02	0.0569	0.0123	20.4	4.4	38.0	63.7	23.1	3.6
total gas												**0.0512**	**0.0184**	**18.4**	**6.6**			**22.3**	**3.6**

Table 4. Diatoms relative abundances in the level close to AVT tephra in cores TR17-12PC and TR17-05PC.

Core ID	TR17-12PC					TR17-05PC					
depth (cm)	*Eucampia antarctica*	*Fragilariopsis curta*	*Thalassiosira antarctica*	others	ADA*10^6 (nv/gds)	depth (cm)	*Eucampia antarctica*	*Fragilariopsis curta*	*Thalassiosira antarctica*	others	ADA*10^6 (nv/gds)
357.5	4.0	33.6	34.9	27.4	105.1	38.5	2.3	66.1	14.2	17.4	2620.8
367.5	4.1	36.3	28.4	31.2	98.5	46.5	8.1	31.0	31.0	29.9	718.8
382.5	13.5	18.4	33.7	34.4	134.4	47.5	3.0	43.7	20.4	32.9	953.9
387.5	1.4	30.7	37.2	30.7	49.0	54.5	4.9	37.5	27.1	30.5	1124.0
392.5	2.1	28.9	36.3	32.7	106.8	57.5	2.9	37.1	13.7	46.3	485.1
397.5	1.0	35.1	31.5	32.5	790.9	58.5	1.5	37.8	28.9	31.9	1670.7
402.5	1.8	32.1	33.8	32.4	191.9	62.5	0.3	39.8	25.5	34.4	745.6
405.5	1.0	34.8	23.2	41.1	100.5	65.5	3.9	21.3	32.8	42.0	289.1
						67.5	3.1	40.4	22.3	34.2	52.7
						68.5	2.2	15.6	31.1	51.1	17.8
						72.5	13.2	16.2	27.9	42.7	30.5
						75.5	3.2	42.6	18.1	36.2	19.5
						77.5	3.2	40.9	22.6	33.3	62.8
						80.5	0.0	14.3	42.9	42.9	3.0
						82.5	4.8	42.9	0.0	52.4	5.9
						86.5	3.4	47.2	16.9	32.6	26.4
						90.5	16.7	33.3	33.3	16.7	2.6
						98.5	3.5	59.1	9.9	27.5	46.9
						103	7.1	50.0	12.5	30.4	21.1
						108	1.6	63.5	12.7	22.2	17.9

1143